

**Special Section:**The Mars Perseverance Rover  
Jezero Crater Floor Campaign**Key Points:**

- Mars Environmental Monitoring Station (MEDA) allows the first in situ determination of the surface radiative budget on Mars, providing key constraints on numerical models
- MEDA allows the direct determination of thermal inertia and albedo, providing ground-truth to satellite retrievals
- Albedo shows a strong non-Lambertian behavior, with minimum values at noon and higher values toward sunrise and sunset

**Supporting Information:**

Supporting Information may be found in the online version of this article.

**Correspondence to:**G. M. Martínez,  
[gmartinez@lpi.usra.edu](mailto:gmartinez@lpi.usra.edu)**Citation:**

Martínez, G. M., Sebastián, E., Vicente-Retortillo, A., Smith, M. D., Johnson, J. R., Fischer, E., et al. (2023). Surface energy budget, albedo and thermal inertia at Jezero Crater, Mars, as observed from the Mars 2020 MEDA instrument. *Journal of Geophysical Research: Planets*, 128, e2022JE007537. <https://doi.org/10.1029/2022JE007537>

Received 17 AUG 2022

Accepted 6 JAN 2023

© 2023 Lunar and Planetary Institute and Jet Propulsion Laboratory, California Institute of Technology. Government sponsorship acknowledged. This article has been contributed to by U.S. Government employees and their work is in the public domain in the USA. This is an open access article under the terms of the [Creative Commons Attribution-NonCommercial-NoDerivs License](https://creativecommons.org/licenses/by/4.0/), which permits use and distribution in any medium, provided the original work is properly cited, the use is non-commercial and no modifications or adaptations are made.

## Surface Energy Budget, Albedo, and Thermal Inertia at Jezero Crater, Mars, as Observed From the Mars 2020 MEDA Instrument

G. M. Martínez<sup>1,2</sup> , E. Sebastián<sup>3</sup>, A. Vicente-Retortillo<sup>2,3</sup> , M. D. Smith<sup>4</sup> , J. R. Johnson<sup>5</sup> , E. Fischer<sup>2</sup> , H. Savijärvi<sup>6</sup> , D. Toledo<sup>7</sup> , R. Hueso<sup>8</sup> , L. Mora-Sotomayor<sup>3</sup> , H. Gillespie<sup>1</sup>, A. Manguira<sup>8</sup> , A. Sánchez-Lavega<sup>8</sup> , M. T. Lemmon<sup>9</sup> , F. Gómez<sup>3</sup> , J. Polkko<sup>10</sup> , L. Mandon<sup>11</sup> , V. Apéstigue<sup>6</sup> , I. Arruego<sup>6</sup> , M. Ramos<sup>12</sup>, P. Conrad<sup>13</sup>, C. E. Newman<sup>14</sup> , M. de la Torre-Juarez<sup>15</sup> , F. Jordan<sup>3</sup>, L. K. Tamppari<sup>15</sup> , T. H. McConnochie<sup>9</sup>, A.-M. Harri<sup>10</sup>, M. Genzer<sup>10</sup>, M. Hieta<sup>10</sup> , M.-P. Zorzano<sup>3</sup>, M. Siegler<sup>16</sup> , O. Prieto<sup>3</sup>, A. Molina<sup>3</sup> , and J. A. Rodríguez-Manfredi<sup>3</sup>

<sup>1</sup>Lunar and Planetary Institute, Universities Space Research Association, Houston, TX, USA, <sup>2</sup>University of Michigan, Ann Arbor, MI, USA, <sup>3</sup>Centro de Astrobiología (INTA-CSIC), Madrid, Spain, <sup>4</sup>NASA Goddard Space Flight Center, Greenbelt, MD, USA, <sup>5</sup>John Hopkins University Applied Physics Laboratory, Laurel, MD, USA, <sup>6</sup>University of Helsinki, Helsinki, Finland, <sup>7</sup>Instituto Nacional de Técnica Aeroespacial, Torrejón de Ardoz, Spain, <sup>8</sup>Universidad del País Vasco, Euskal Herriko Unibertsitatea, Leioa, Spain, <sup>9</sup>Space Science Institute, Boulder, CO, USA, <sup>10</sup>Finnish Meteorological Institute, Helsinki, Finland, <sup>11</sup>Laboratoire d'Etudes Spatiales et d'Instrumentation en Astrophysique, Observatoire de Paris-PSL, Paris, France, <sup>12</sup>Universidad de Alcalá de Henares, Alcalá de Henares, Spain, <sup>13</sup>Carnegie Institution for Science, Washington, DC, USA, <sup>14</sup>Aeolis Research, Chandler, AZ, USA, <sup>15</sup>Jet Propulsion Laboratory, California Institute of Technology, Pasadena, CA, USA, <sup>16</sup>Planetary Science Institute, Tucson, AZ, USA

**Abstract** The Mars Environmental Dynamics Analyzer (MEDA) on board Perseverance includes first-of-its-kind sensors measuring the incident and reflected solar flux, the downwelling atmospheric IR flux, and the upwelling IR flux emitted by the surface. We use these measurements for the first 350 sols of the Mars 2020 mission ( $L_s \sim 6^\circ\text{--}174^\circ$  in Martian Year 36) to determine the surface radiative budget on Mars and to calculate the broadband albedo ( $0.3\text{--}3\ \mu\text{m}$ ) as a function of the illumination and viewing geometry. Together with MEDA measurements of ground temperature, we calculate the thermal inertia for homogeneous terrains without the need for numerical thermal models. We found that (a) the observed downwelling atmospheric IR flux is significantly lower than the model predictions. This is likely caused by the strong diurnal variation in aerosol opacity measured by MEDA, which is not accounted for by numerical models. (b) The albedo presents a marked non-Lambertian behavior, with lowest values near noon and highest values corresponding to low phase angles (i.e., Sun behind the observer). (c) Thermal inertia values ranged between 180 (sand dune) and 605 (bedrock-dominated material) SI units. (d) Averages of albedo and thermal inertia (spatial resolution of  $\sim 3\text{--}4\ \text{m}^2$ ) along Perseverance's traverse are in very good agreement with collocated retrievals of thermal inertia from Thermal Emission Imaging System (spatial resolution of 100 m per pixel) and of bolometric albedo in the  $0.25\text{--}2.9\ \mu\text{m}$  range from (spatial resolution of  $\sim 300\ \text{km}^2$ ). The results presented here are important to validate model predictions and provide ground-truth to orbital measurements.

**Plain Language Summary** We analyzed first-of-its-kind measurements from the weather station on board NASA's Perseverance rover. These include the incident solar radiation and the amount that is reflected by the surface, as well as the thermal atmospheric forcing (greenhouse effect) and the thermal heat released by the surface. These measurements comprise the radiant energy budget, which is fundamental to understanding Mars' weather through its impact on temperatures. From the solar measurements, we obtained the surface reflectance for a variety of illuminating and viewing geometries. We found that the thermal atmospheric forcing is weaker than expected from models, likely because of the strong diurnal variation in atmospheric aerosols observed by the rover, which is not accounted for by models. We also found that the surface reflectance is not uniform from all directions, but that it decreases when the Sun is highest in the sky (near noon) and increases when the Sun is directly behind the observer (sunset and sunrise), and thus the shadows cast by their roughness elements (e.g., pores and pits) are minimized. Because models neither consider diurnal variations in atmospheric aerosols nor in the surface reflectance, the results presented here are important to validate model predictions for future human exploration.

**Author Contributions:**

**Conceptualization:** G. M. Martínez, H. Savijärvi, R. Hueso, H. Gillespie, A. Munguira, M. Ramos, P. Conrad  
**Data curation:** G. M. Martínez, E. Sebastián, A. Vicente-Retortillo, M. D. Smith, D. Toledo, L. Mora-Sotomayor, M. T. Lemmon, J. Polkko, L. Mandon, V. Apéstigue, I. Arruero, F. Jordan, A.-M. Harri, M. Genzer, M. Hieta  
**Formal analysis:** G. M. Martínez, E. Sebastián, A. Vicente-Retortillo, J. R. Johnson, E. Fischer, H. Savijärvi, R. Hueso, A. Munguira, A. Sánchez-Lavega, F. Gómez  
**Funding acquisition:** G. M. Martínez, M. de la Torre-Juarez  
**Investigation:** G. M. Martínez, C. E. Newman, M. de la Torre-Juarez, L. K. Tamppari, T. H. McConnochie, M.-P. Zorzano, M. Siegler, O. Prieto, A. Molina, J. A. Rodríguez-Manfredi  
**Methodology:** G. M. Martínez, E. Sebastián, A. Vicente-Retortillo, M. D. Smith, J. R. Johnson, E. Fischer, D. Toledo, H. Gillespie, A. Sánchez-Lavega, M. T. Lemmon  
**Project Administration:** G. M. Martínez, J. A. Rodríguez-Manfredi  
**Resources:** G. M. Martínez  
**Software:** G. M. Martínez  
**Supervision:** G. M. Martínez  
**Validation:** G. M. Martínez, E. Sebastián, A. Vicente-Retortillo, M. D. Smith, J. R. Johnson, D. Toledo, L. Mora-Sotomayor, M. T. Lemmon, J. Polkko, L. Mandon, V. Apéstigue, I. Arruero, F. Jordan  
**Visualization:** G. M. Martínez  
**Writing – original draft:** G. M. Martínez, E. Sebastián, A. Vicente-Retortillo, J. R. Johnson  
**Writing – review & editing:** G. M. Martínez, E. Sebastián, M. D. Smith, J. R. Johnson, E. Fischer, D. Toledo, R. Hueso, A. Sánchez-Lavega, F. Gómez, M. Ramos

**1. Introduction**

The Mars 2020 Perseverance rover landed at Jezero Crater (77.5945°E, 18.3628°N, −2,656 m) on 18 February 2021, corresponding to a solar longitude ( $L_s$ ) of  $\sim 5^\circ$  in the Martian Year (MY) 36. It carries seven science instruments to fulfill four science goals: (a) understand the geology of the landing site, (b) identify ancient habitable environments and look for preserved biosignatures, (c) collect and document samples for future Earth return, and (d) enable future human exploration of Mars (Farley et al., 2020).

Among these instruments, the Mars Environmental Monitoring Station (MEDA) is a meteorological station selected by NASA to help achieve mission science goal 4 (Newman et al., 2022; Rodríguez-Manfredi et al., 2021). In particular, the main programmatic objectives of MEDA are to (a) validate global atmospheric models by taking surface weather measurements and (b) characterize dust size and morphology to understand its effects on the operation of surface assets and human health. Additionally, MEDA provides environmental context in support of science goals 1–3 and the flights of Ingenuity, the helicopter included in the mission as a technology demonstrator.

To achieve its objectives, MEDA carries six sensor packages: the Thermal Infrared Sensor (TIRS, Pérez-Izquierdo et al., 2018; Sebastián et al., 2020, 2021), the Radiation and Dust Sensor (RDS, Apéstigue et al., 2022), the Atmospheric Temperature Sensor (ATS), the Pressure Sensor (PS), the Relative Humidity Sensor (HS), and the Wind Sensor (WS). In addition, the RDS incorporates an upward-viewing wide-angle camera to image the sky, informally called SkyCam. Among these, TIRS and RDS provide first-of-its-kind measurements from the surface of Mars, and are the main focus of this article.

RDS and TIRS allow the determination of the surface radiative budget on Mars for the first time through measurements of the incident ( $SW_d$ , 0.19–1.2  $\mu\text{m}$ ) and reflected ( $SW_r$ , 0.3–3  $\mu\text{m}$ ) solar flux, the downwelling atmospheric IR flux ( $LW_d$ , 6.5–30  $\mu\text{m}$ ), and the upwelling IR flux emitted by the surface ( $LW_u$ , 6.5–30  $\mu\text{m}$ ). As required in quantifications of the radiative energy budget, we explain in Section 3 how to extend these measurements to the entire shortwave (0.19–5) and longwave range (5–80  $\mu\text{m}$ ). The surface radiative budget of Mars is fundamental to understanding its weather and climate through its impact on the thermal structure and atmospheric circulations (e.g., Creedy et al., 2022). Moreover, RDS and TIRS measurements are critical to validate and improve predictive capabilities of numerical models. Therefore, the determination of the surface radiative budget is critical to achieve MEDA's first programmatic objective. Before Perseverance, this budget has been estimated using a combination of in situ measurements and numerical models (G. M. Martínez et al., 2021, and references therein). Here, we expand and improve upon previous studies by analyzing in situ measurements of the surface radiative budget around the clock.

Together with the radiative fluxes, the turbulent heat flux ( $H_0$ ) and the latent heat flux ( $L_f$ ) make up the surface energy budget (SEB), which can be expressed as  $G = SW_d - SW_u + LW_d - LW_u - H_0 - L_f$  (Garrat, 1992). Here,  $G$  represents the net heat flux into the ground, and  $R_n = SW_d - SW_u + LW_d - LW_u$  is the net radiative flux derived from MEDA measurements (sign convention defined in Section 3). Although not measured,  $H_0$  and  $L_f$  can be estimated using combined MEDA measurements from TIRS, ATS, WS, PS, and HS using similarity theories (Section 3). These two terms play, at most, a minor role in the Martian SEB (Haberle et al., 1993; G. M. Martínez et al., 2014, 2021; H. I. Savijärvi et al., 2022; Sutton et al., 1978). Therefore, MEDA provides a reasonable approximation to the SEB at Jezero.

Another novel capability of MEDA is the direct determination of the broadband (0.3–3  $\mu\text{m}$ ) albedo through measurements of the incident and reflected solar flux (see Section 3.2 for the definition of albedo used in this article). Albedo is a key parameter in the radiative energy budget, thus affecting the local weather and climate (Fenton et al., 2007; Kahre et al., 2005). In previous surface-based missions, the albedo has been calculated either from radiometrically calibrated images taken by panoramic cameras (Bell et al., 2008; Rice et al., 2018), or by using numerical models to best fit observed values of ground temperature (Piqueux et al., 2021; Vasavada et al., 2017). Additionally, telescope and satellite observations have been used to retrieve albedo globally across the planet (e.g., Christensen, 1988; Christensen et al., 2001; Kieffer et al., 1977; Vincendon et al., 2015). In either case, the temporal coverage was limited given the nature of the observations, with one image or satellite retrieval per day and location at best. Accordingly, the geometry of incident and reflected solar fluxes was limited, complicating assessments of the Lambertian (isotropically scattering surface) approximation, which has been assumed in these studies.

Here, we expand upon previous studies and obtain broadband albedo values for a variety of illumination and viewing geometries, which allows us to study the degree to which the surface materials depart from ideal Lambertian scattering (Section 4). This is important for improving predictive capabilities of mesoscale and global models (Fenton et al., 2007; Montmessin et al., 2007), which typically incorporate albedo variations in subseasonal time scales (Fenton et al., 2007; Geissler et al., 2016; Haberle et al., 1993; Kahre et al., 2005), but not in diurnal timescales arising from non-Lambertian behavior. Similarly, surface-based and satellite retrievals of thermal inertia (R. L. Fergason, Christensen, & Kieffer, 2006; Piqueux et al., 2021; Putzig et al., 2005; H. Savijärvi et al., 2020; Vasavada et al., 2017) typically consider a constant value of albedo throughout the day, and thus may also benefit from non-Lambertian considerations.

Furthermore, MEDA measurements allow for the direct estimation of thermal inertia assuming homogeneous terrains within the ground temperature sensor's field of view (Section 3). Thermal inertia is an important geophysical property of the terrain, which modulates the amount of energy flux that is transported into the subsurface, and thus determines surface and shallow subsurface temperatures. In previous studies, thermal inertia has been obtained by fitting thermal models to measurements of ground temperature retrieved from satellite observations (e.g., R. Fergason et al., 2012; R. L. Fergason, Christensen, & Kieffer, 2006; Kieffer et al., 1977; Mellon et al., 2000), measured by surface-based missions (e.g., R. L. Fergason, Christensen, Bell, et al., 2006; Hamilton et al., 2014; G. M. Martínez et al., 2014; Piqueux et al., 2021; Vasavada et al., 2017), or using both data sets coincidentally (Christian et al., 2022; Edwards et al., 2018). In either case, a thermal model is fed with key parameters such as aerosol opacity, pressure, and albedo, among others, to simulate the SEB at the surface. Then, these models solve the heat conduction at the ground for homogeneous or heterogeneous terrains using the simulated SEB as the upper boundary condition, obtaining the thermal inertia by best fitting their outputs to measured values of ground temperature.

Here we obtain thermal inertia directly by using MEDA measurements of ground temperature ( $T_g$ ), albedo and SEB assuming homogeneous terrains. An in-depth analysis of the differences between thermal inertia values derived assuming heterogeneous versus homogeneous terrains is presented in H. I. Savijärvi et al. (2022).

In this article, we report results of the surface energy budget, broadband albedo, and thermal inertia for the first 350 sols of the M2020 mission, corresponding to  $L_s$  6°–174° in MY 36. The structure of the article is as follows: Section 2 describes MEDA observations with a focus on TIRS and RDS. Section 3 explains the methods to calculate each term of the surface energy budget (Section 3.1), albedo (Section 3.2), and thermal inertia (Section 3.3). Section 4 shows the results, and it is also divided into three subsections devoted to the thermal inertia (Section 4.1), surface energy budget (Section 4.2), and albedo (Section 4.3). Section 5 discusses discrepancies between measured and modeled values of the downwelling atmospheric IR flux. Section 6 contains the summary and conclusions.

## 2. The MEDA Instrument

Here, we explain the measuring strategy of MEDA and describe each of its six sensor packages, with a focus on TIRS and RDS.

The nominal measuring strategy of MEDA began on sol 15 ( $L_s \sim 12^\circ$ ). It consists of 1h-and-5'-long blocks starting at odd Local Mean Solar Times (LMST) hours on odd sols, and on even LMST hours on even sols (Figure 1). This ensures that the beginning of each hour is covered on every sol, and that each full hour is covered every two sols. Additional or extended blocks are added when mission resources allowed (data volume and power). During nominal or extended blocks, each MEDA sensor is typically measuring at 1 Hz, although a higher frequency of 2 Hz has been used occasionally by a few sensors (e.g., ATS) to better characterize turbulent phenomena. In parallel, a few SkyCam images are taken on each sol (typically between 3 and 4).

TIRS is the first in situ Martian IR radiometer including upward- and downward-looking channels (Pérez-Izquierdo et al., 2018; Sebastián et al., 2020, 2021). TIRS measures the downwelling atmospheric IR flux (IR1), the air temperature from an atmospheric layer with peak emission at 40 m (IR2, Smith et al., 2006), the reflected (upwelling) solar flux (IR3), the upwelling IR flux emitted by the surface (IR4), and the surface brightness temperature (IR5) (Table 1). IR1, IR2, IR3, and IR4 provide novel measurements on Mars, while IR5 complements previous measurements of surface brightness temperatures taken by the Rover Environmental Monitoring

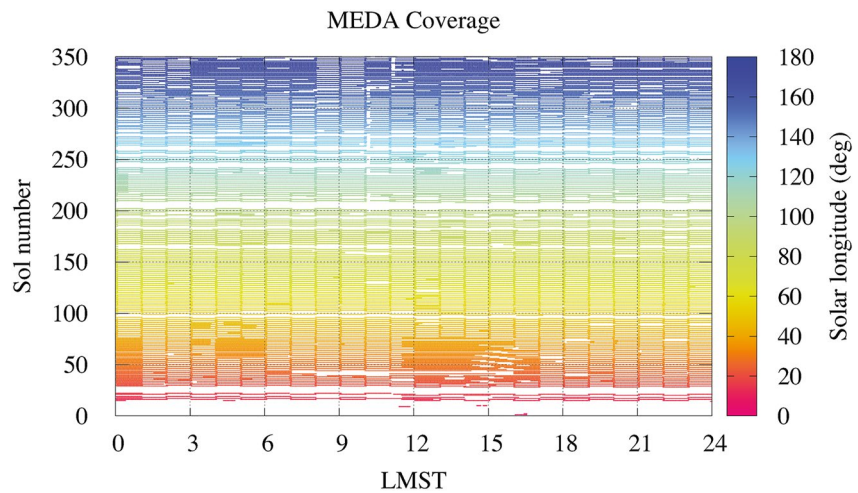


**Figure 1.** Temporal coverage of Mars Environmental Monitoring Station (MEDA) as a function of Local Mean Solar Times (LMST) and sol number, with Ls shown with color code. Sols with no coverage correspond to periods when MEDA was off due to various reasons, while the dense cloud of reddish points between 11:00 and 17:00 LMST in sols 31–77 corresponds to extra measurements taken in support of the first Ingenuity flights.

Station (REMS) on board the Mars Science Laboratory (MSL) mission (Sebastián et al., 2010), and by the HP<sup>3</sup> instrument on board InSight (Spohn et al., 2018).

TIRS is mounted on the rover sensing mast (RSM) at a height of 1.5 m, and it is located 75° clockwise in the horizontal plane with respect to Z-axis local frame (with +X defined along the forward direction and +Y pointing to the right of the rover). The field of view (FoV) of the downward-looking channels covers an ellipsoid area of 3–4 m<sup>2</sup>, whose center is ~3.75 m away from the M2020 Radioisotope Thermoelectric Generator to avoid thermal contamination (Figure 2). Most of the signal comes from the central part of the ellipsoid, where the detectors have the highest responsivity (Sebastián et al., 2020). Due to the smaller area covered by TIRS as compared with the MSL/REMS ground temperature sensor (3–4 vs. ~100 m<sup>2</sup>), lateral heterogeneities in thermal inertia and albedo are expected to be more prevalent at the MSL than at the M2020 landing site.

The RDS is located on the rover deck (Figure 2). It includes 16 photodiodes and the SkyCam to take images of the sky in the 0.6–0.8 μm range (Apéstigue et al., 2022). Among the 16 photodetectors, eight point toward the zenith (TOP) in different spectral bands ranging from the UV to the near IR, while eight point sideways (LAT) in the 0.75 ± 0.01 μm range, each separated 45° from the next in the horizontal plane to cover 360°. The LAT1 sensor is blinded, and it is used to evaluate possible photodetector degradation. RDS TOP photodetectors complement and expand upon previous solar flux measurements taken by the MSL/REMS instrument, which

**Table 1**  
*Specifications and Geometrical Description of Thermal Infrared Sensor*

Channel	IR1	IR2	IR3	IR4	IR5
Measurement	$LW_d$	$T_a$	$SW_u$	$LW_u$	$T_g$
Band (μm)	6.5–30	14.5–15.5	0.3–3	6.5–30	8–14
Field of view	±20°H and ±10°V	±20°H and ±10°V	±20°H and ±10°V	±20°H and ±10°V	±20°H and ±10°V
Pointing angle	+35°	+35°	–35°	–35°	–35°
Accuracy	<6.9 W/m <sup>2</sup>	±2.83 K	<9.6 W/m <sup>2</sup>	<3.3 W/m <sup>2</sup>	±0.75 K
Resolution	±0.18 W/m <sup>2</sup>	±0.45 K	±0.1 W/m <sup>2</sup>	±0.13 W/m <sup>2</sup>	±0.08 K

*Note.*  $LW_d$  is the downwelling atmospheric IR flux,  $T_a$  is the air temperature at about 40 m,  $SW_u$  is the solar flux reflected by the surface,  $LW_u$  is the upwelling IR flux emitted by the surface, and  $T_g$  is the surface brightness temperature. For the accuracy and resolution of IR1 and IR4, a hemispherical field of view and the full IR range was considered in preflight calibrations (Sebastián et al., 2020, 2021). For IR3, a hemispherical field of view was also considered based on laboratory and field calibrations (Rodríguez-Manfredi et al., 2021).

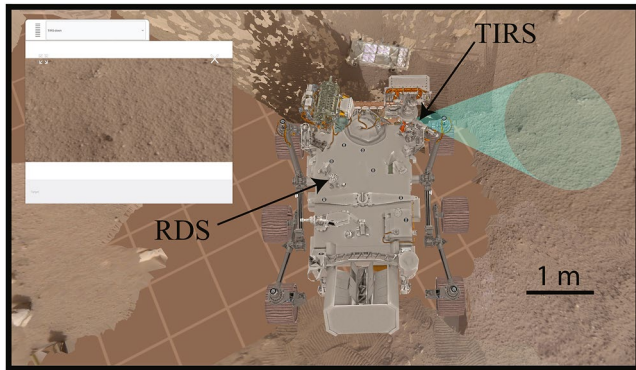


**Figure 2.** The field of view of the downward-looking Thermal Infrared Sensor (TIRS) channels IR3, IR4, and IR5 (shaded green area) on sol 30. For terrains with no tilt, it covers an ellipsoidal area of  $\sim 3\text{--}4\text{ m}^2$ . The arrows point toward the location of TIRS on the remote sensing mast, which is placed  $75^\circ$  clockwise from the rover forward direction, and of the Radiation and Dust Sensor on the rover deck. A zoomed-in view of the TIRS' field of view is shown in the top left insert.

only cover the UV range (Vicente-Retortillo et al., 2020). SkyCam has a strong heritage from the hazard cameras (HazCams) used in the MSL and Mars Exploration Rover (MER) missions (J. Maki et al., 2012; J. N. Maki et al., 2003).

Among the 16 RDS photodiodes, here we only use measurements from the panchromatic channel (TOP 7), which measures the downwelling solar flux in the  $0.19\text{--}1.2\text{ }\mu\text{m}$  range with a hemispherical FoV of  $\pm 90^\circ$ , and with an accuracy and resolution of 5.6% and  $0.0221\text{ W m}^{-2}$ , respectively. The reader is referred to Toledo et al. (2023) for the science results of RDS using TOP and LAT channels combined.

Measurements of TIRS/IR1 ( $LW_d$ ), TIRS/IR3 ( $SW_d$ ), TIRS/IR4 ( $LW_d$ ), and RDS/TOP7 ( $SW_d$ ) allow the determination of the net radiative energy budget,  $R_n$ . In addition, we use measurements from other MEDA sensors to provide environmental context and to estimate the turbulent heat flux. We briefly describe each of these sensors below.

The ATS includes five atmospheric sensors based on thermocouples. Three of them (ATS1, ATS2, and ATS3) are located on the RSM at 1.45 m above the ground, separated  $\sim 120^\circ$  from each other in the horizontal plane to ensure that at least one is always upwind from rover thermal interferences. Two other

thermocouples (ATS 4 and ATS5) are attached to the sides of the rover at a height of 0.84 m. All thermocouples have an accuracy and resolution better than 1 and 0.01 K, respectively (Rodríguez-Manfredi et al., 2021). Here, we use measurements from ATS1, ATS2 and ATS3, which typically provide similar values and are less affected by the contamination from the rover (Munguira et al., 2022).

The WS consists of two booms located on the RSM at  $\sim 1.5\text{ m}$  height, separated  $\sim 120^\circ$  from each other in the horizontal plane to mitigate rover hardware interferences (Rodríguez-Manfredi et al., 2021). Data from both booms are combined to produce horizontal wind speed and direction values of the highest confidence, with accuracies of  $\pm 1\text{ m/s}$  and a resolution of 0.5 m/s for wind speeds  $< 10\text{ m/s}$ , and 10% of the measurement and 0.1 m/s for wind speeds between 10 and 40 m/s. The WS was damaged by a dust devil during the regional dust storm around sols 312–318 ( $L_s 152^\circ\text{--}156^\circ$ ) (Hueso et al., 2022; Lemmon et al., 2022; Viúdez-Moreiras, de la Torre, et al., 2022; Viúdez-Moreiras, Lemmon, et al., 2022). Thus, WS measurements of the highest confidence are only available for the first 313 sols of the mission (Figure S1 in Supporting Information S1). In addition, the wind sensor had to be turned off during orbital communication passes, which reduces its time coverage compared to other MEDA sensors (Figure S1 in Supporting Information S1).

The PS is located in a temperature-controlled box inside the rover, and it is connected to the atmosphere through a pipe (Rodríguez-Manfredi et al., 2021; Sánchez-Lavega et al., 2022). It measures the atmospheric pressure with an estimated accuracy  $\sim 3.5\text{ Pa}$  and a resolution of 0.13 Pa. In combination with the ATS, these sensors can be used to estimate the atmospheric density, which is an important quantity in support of the Mars Oxygen In-Situ Resource Utilization Experiment (MOXIE) instrument on board M2020, and also to estimate the turbulent heat flux (Section 3).

The HS is located on the RSM at 1.5 m height from the ground (Hieta et al., 2022), and it was calibrated to provide values of the relative humidity (RH) with respect to ice with uncertainty lower than 4.5% for temperatures above 203 K, and lower than 6% down to 190 K. The precision of the HS is better than 0.02% in RH. Due to some inflight maintenance, only HS measurements taken after sol 80 ( $L_s \sim 43.5^\circ$ ) are suitable for scientific investigations. The HS can also be used to estimate the water vapor pressure at 1.5 m as  $e = \text{RH} \times e_s(T_b)$ , where  $T_b$  is the temperature of the HS measured directly from the HUMICAP chip, and  $e_s$  is the saturation vapor pressure over ice (H. Savijärvi & Määttä, 2010). Similarly, the water vapor volume mixing ratio can be estimated as  $\text{VMR} = e/P = (\text{RH} \times e_s(T_b))/P$ , where  $P$  is the atmospheric pressure provided by the PS. In both cases,  $e$  and  $\text{VMR}$  can be obtained reliably only when  $\text{RH} > 2\%$ , roughly corresponding to LMST between 07:00 and 17:00 (Figure S2g in Supporting Information S1). The reader is referred to Hieta et al. (2022) for further details on the science capabilities of the HS.

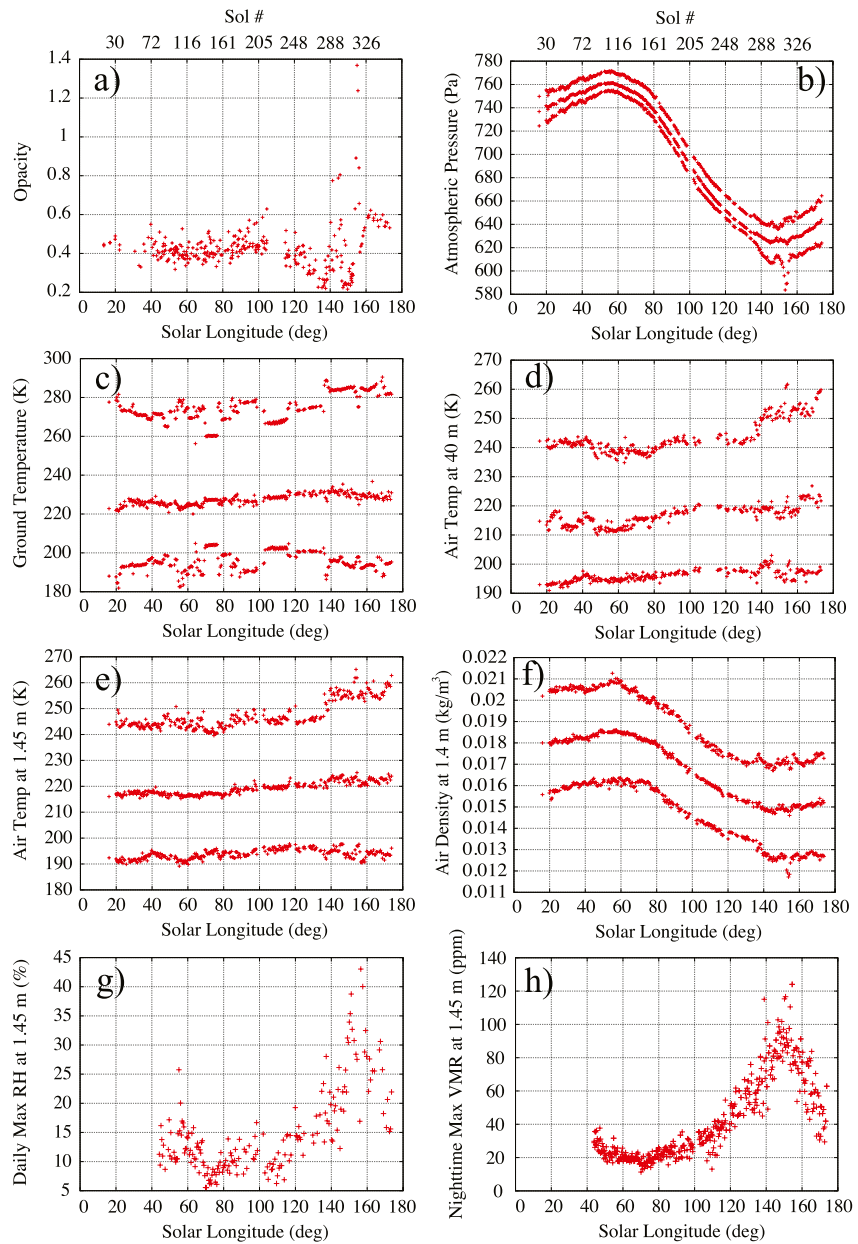


**Figure 3.** Environmental conditions during the first 350 sols of the M2020 mission, which roughly cover the entire Martian aphelion season. (a) Aerosol opacity at  $0.88 \mu\text{m}$  retrieved by the Mastcam-Z instrument. (b) Daily maximum, mean, and minimum atmospheric pressure. (c) Daily maximum, mean, and minimum ground temperature. (d) Daily maximum, mean, and minimum air temperature at about 40 m. (e) Daily maximum, mean, and minimum air temperature at 1.45 m, where only ATS1, ATS2, and ATS3 have been considered. (f) Daily maximum, mean, and minimum atmospheric density at 1.45 m. (g) Daily maximum relative humidity. (h) Nighttime maximum water vapor VMR.

To provide context for the results shown in Section 4, Figure 3 shows the subseasonal evolution of the environmental conditions across Perseverance's traverse for the first 350 sols of the M2020 mission. Diurnal variations of the same quantities are shown in Figure S2 in Supporting Information S1.

### 3. Methods

In this section, we explain the methods to calculate each term of the surface energy budget (Section 3.1), hemispheric albedo (Section 3.2), and thermal inertia (Section 3.3) using MEDA observations.

### 3.1. Surface Energy Budget

The surface energy budget can be expressed as

$$G = (SW_d - SW_u + LW_d - LW_u) - (H_0 + L_f), \quad (1)$$

where  $G$  represents the net heat flux into the ground,  $R_n = SW_d - SW_u + LW_d - LW_u$  the net surface radiative flux, and  $H_0$  and  $L_f$  the turbulent and latent heat flux. Following the convention in Garrat (1992), radiative fluxes are plugged into this equation as positive values, whereas  $H_0$  and  $L_f$  fluxes can be plugged in as positive or negative depending on whether they are directed away (cooling) from or toward (warming) the surface, respectively.

The spectral boundary between solar ( $SW_d$  and  $SW_u$ ) and IR ( $LW_d$  and  $LW_u$ ) fluxes are set at 5  $\mu\text{m}$  (Wolff et al., 2017), which may cause inaccuracies smaller than 0.5% in the individual terms; this effect is in turn partially compensated due to the subtraction of downwelling and upwelling terms.

#### 3.1.1. Shortwave Flux

##### 3.1.1.1. Downwelling Solar Flux: RDS/TOP7

The most processed RDS/TOP7 measurements available in the NASA Planetary Data System (PDS) are “Calibrated Data” (\*CAL\_RDS\* files). To obtain  $SW_d$  from these measurements, we took the following steps: (a) correction for the angular response, (b) extension from 0.19–1.2  $\mu\text{m}$  to 0.19–5  $\mu\text{m}$  (atmospheric  $\text{CO}_2$  blocks wavelengths  $<0.19 \mu\text{m}$ ; e.g., Vicente-Retortillo et al., 2015), and (c) correction for the amount of dust deposited on the photodiode. Moreover, we discard measurements: (d) affected by shadows cast by the RSM, and (e) taken when the RDS/TOP7 was saturated.

The angular response of the RDS/TOP7 channel is available in the Supporting Information S1 in the form of a look-up table as a function of the aerosol opacity ( $\tau$ ) and solar zenith angle ( $SZA$ ) stored in ASCII format (Data Set S1). Aerosol opacity values (Figure 3a and Figure S2a in Supporting Information S1) are available in the Data Availability Statement, while  $SZA$  values are available in the PDS as “Derived Data” (\*DER\_ANCIL-LARY\* files). To convert RDS/TOP7 fluxes from 0.19–1.2 to 0.19–5  $\mu\text{m}$ , we use a look-up table (available in Supporting Information S1 in ASCII format; Data Set S2, seventh column) generated by our COMIMART radiative model (Vicente-Retortillo et al., 2015), which also depends on the aerosol opacity and, more modestly, on the  $SZA$ . Finally, we quantify the effect of dust deposited on the RDS/TOP7 through the calculation of a dust correction factor (DCF). This quantity is defined as the fraction of the incoming flux that reaches the photodiode through dust accumulated on the sensor, with respect to the fraction at the beginning of the mission. By using COMIMART fed with aerosol opacity retrieved from Mastcam-Z, RDS/TOP7 measurements, and the methodology developed in Vicente-Retortillo et al. (2018, 2020), we estimated an averaged DCF of 0.94 over the first 270 sols of the mission (i.e., 94% of the solar flux is transmitted through the dust accumulated on the window of the sensor). Interestingly, the DCF stayed reasonably constant at 0.94 throughout this period ( $L_s$  in  $6^\circ$ – $130^\circ$ ), including the first sols of the mission. This suggests that some dust might have deposited on the RDS/TOP7 window during landing. This hypothesis is further supported by an in-flight recalibration of TIRS performed during the first few sols, which resulted in a degradation of  $\sim 9\%$  in the signal measured by the upward-looking TIRS channels.

In addition to the corrections explained above, we discard measurements affected by shadows cast by the RSM. At the time of this writing, there are no flags available in the “CAL\_RDS” files indicating whether or not an RDS/TOP7 measurement is affected by such shadows. Thus, we discard these measurements manually from visual inspection. Moreover, we discard measurements when the RDS/TOP7 was saturated, which can occur under two different scenarios: in the vicinity of sunrise when the RDS was operating in high gain mode and in the vicinity of noon between sols  $\sim 270$  ( $L_s \sim 131^\circ$ ) and 350 ( $L_s \sim 174^\circ$ ) when the incident solar flux was higher than the upper bound of the range established in preflight calibrations on Earth (Figure S3 in Supporting Information S1). During this period (sols 270–350), we used COMIMART fed with aerosol opacity values from Mastcam-Z to simulate near-noon values of  $SW_d$  (more details in Section 3.2). As with the shadows, there are no flags associated with saturated measurements of either kind and we discarded them manually.

After the completion of the five steps defined in the first paragraph, we use RDS/TOP7 measurements to produce averaged values at the beginning of each hour on every sol, and at each half of the hour on every two sols. In each case, the averaging period is 5 min. This strategy nominally results in 36 sub-hourly values per sol: 24 at the

beginning of each hour and 12 at every half of the hour. For consistency, we apply the same averaging method to every MEDA observed or derived quantity used in this article.

### 3.1.1.2. Upwelling Flux Reflected by the Surface: TIRS/IR3

The most processed TIRS/IR3 data set available in the PDS is “Calibrated Data” (\*CAL\_TIRS\* files), which provides values of the reflected solar flux in the 0.3–3  $\mu\text{m}$  band for a hemispherical FoV (Sebastián et al., 2020, 2021). To calculate  $SW_u$ , we convert these fluxes to 0.2–5  $\mu\text{m}$  by using a look-up table generated by our COMIMART model (Data Set S2).

In the \*CAL\_TIRS\* measurements, there are associated flags indicating whether there are shadows cast by the RSM or the rover body in the FoV of the TIRS downward-looking channels (IR3–5, Table 1). In this work, we keep track of this flag to account for the existence or lack of shadows among all TIRS/IR3 measurements.

### 3.1.2. Longwave Flux

TIRS measures  $LW_d$  and  $LW_u$  in the 6.5–30  $\mu\text{m}$  range (Table 1). As required in quantifications of the radiative and surface energy budget, we explain next how we extend these measurements to the entire longwave range (5–80  $\mu\text{m}$ ).

#### 3.1.2.1. Downwelling Atmospheric Flux: TIRS/IR1

$LW_d$  values in the 6.5–30  $\mu\text{m}$  range are available in the PDS as “Calibrated Data” (\*CAL\_TIRS\* files), while extended  $LW_d$  values in the 5–80  $\mu\text{m}$  range are available as “Derived Data” (\*DER\_TIRS\* files). Therefore, “DER” files contain the highest-order products for TIRS/IR1.

Following in-flight recalibrations and improved procedures developed during the first year of operations of Perseverance, updated “DER”  $LW_d$  values will be first made available in the PDS on 21 November 2022, and will cover the first 539 sols of the mission. We show these updated values in this article for the first 350 sols ( $L_s \sim 6^\circ$ – $174^\circ$  in MY 36). Therefore, PDS users should ignore “DER”  $LW_d$  values made available in the PDS prior to 21 November 2022.

The main complexity in converting  $LW_d$  values from 6.5–30 to 5–80  $\mu\text{m}$  is that the emission spectrum of the atmosphere cannot be accurately approximated to that of a blackbody. Instead, it is mainly determined by the strong emission of  $\text{CO}_2$  at 15  $\mu\text{m}$  (IR2), and the dust emission spectrum across the LW range. Following these considerations, we used “CAL”  $LW_d$  values, IR2 measurements of temperature and irradiance in the 14.5–15.5  $\mu\text{m}$  range and the spectral responses of IR1 and IR2 (Sebastián et al., 2020) to convert “CAL” to “DER”  $LW_d$  values. From these three data sets, the temporal evolution of the ratio between the radiative fluxes measured by the IR1 and IR2 channels is calculated and compared to that simulated with the University of Helsinki/Finnish Meteorological Institute Single Column Model (hereinafter called SCM) for different values of aerosol optical depth model (H. I. Savijärvi & Harri, 2021). Following this comparison, an estimate of the diurnal evolution of atmospheric aerosol opacity is obtained. Then, we use observations of the atmospheric spectra in the 5–29  $\mu\text{m}$  range measured by Mini-TES for different aerosol opacities and atmospheric temperature profiles (Smith et al., 2006) to obtain a linear function, which is used to convert “CAL” into “DER”  $LW_d$  values as a function of opacity and measured atmospheric temperature. Finally, we convert radiance measured at a fixed elevation angle ( $+35^\circ$ ; Table 1) to that corresponding to a hemispherical FoV by using the diffusivity-factor approximation (Elsasser, 1942). This methodology will be presented in a standalone article, which is currently in preparation.

Both in the “CAL\_TIRS” and “DER\_TIRS” files, there is a flag indicating whether the Sun is in the FoV of the upward-looking channels IR1 and IR2. We discard these measurements, as they result in values that are unrealistically high. Additionally, TIRS has performed several in-flight recalibrations during the first 350 sols of the mission, during which “CAL\_TIRS” and “DER\_TIRS” measurements were affected by controlled, artificial heating of the thermal plate. We discard these measurements too. The complete list of sols and LMST when these recalibrations were performed is available in Data Set S3.

#### 3.1.2.2. Upwelling Flux Emitted by the Surface: TIRS/IR4

$LW_u$  values in the 6.5–30  $\mu\text{m}$  range are available in the PDS as “Calibrated Data” (\*CAL\_TIRS\* files), while extended  $LW_u$  values in the 5–80  $\mu\text{m}$  range are available as “Derived Data” (\*DER\_TIRS\* files).

To convert “CAL” to “DER”  $LW_u$  values, we took the following steps: (a) derivation of an equivalent surface brightness temperature for the ground ( $T_{b\_IR4}$ ) using “CAL”  $LW_u$  measurements, the calibration equations obtained

during preflight calibrations (Sebastián et al., 2020, 2021), and the blackbody assumption for the ground (surface unit emissivity,  $\epsilon$ ), and (b) calculation of  $LW_u$  in the 5–80  $\mu\text{m}$  range by using Stefan-Boltzmann emission law as  $LW_u = \sigma \times T_{b,IR4}^4$ , where  $\sigma = 5.67 \times 10^{-8} \text{ W m}^{-2} \text{ K}^{-4}$  is the Stefan Boltzmann constant.

This methodology represents a simplification because the surface spectral emissivity,  $\epsilon(\lambda)$ , varies across the 5–80  $\mu\text{m}$  range, as observed by Mini-TES in the  $\sim 7\text{--}25 \mu\text{m}$  range (Hamilton et al., 2014). To quantify the error in assuming unit emissivity, we have performed sensitivity studies using  $\epsilon(\lambda)$  values measured by Mini-TES. Results of this analysis yield relative errors in “DER”  $LW_u$  values of up to 3% for an equivalent surface brightness temperature of  $\sim 290 \text{ K}$ , and up to 6% for an equivalent surface brightness temperature of  $\sim 180 \text{ K}$ .

Similar to  $SW_u$ , there are flags in the “CAL” and “DER” files indicating whether there are shadows in the FoV of TIRS/IR4. Here, we consider all measurements, accounting for the existence or lack of shadows by keeping track of this flag. For  $LW_u$ , we discard measurements taken during in-flight recalibration activities (Data Set S3).

### 3.1.3. Turbulent and Latent Heat Flux

The turbulent or sensible heat flux is defined as  $H_0 = \rho c_p \left( \overline{w'T'} \right)_s$  (e.g., Garrat, 1992), where  $\rho$  is the air density,  $c_p = 736 \text{ J kg}^{-1} \text{ K}^{-1}$  is the specific heat of  $\text{CO}_2$  gas at constant pressure, and  $\left( \overline{w'T'} \right)_s$  is the kinematic heat flux, defined as the covariance between the turbulent departures of air temperature,  $T'$ , and vertical wind speed,  $w'$ . The symbol “s” stands for near-surface heights in which the kinematic heat flux is constant, while the overbar denotes an averaging period of a few minutes such that departures from the mean in temperature and vertical wind speed fall within the turbulent spectral range (e.g., Banfield et al., 2020).

While turbulent departures in temperature can be analyzed using measurements from the ATS (Munguira et al., 2022) and SuperCam microphone (Chide et al., 2022), neither the vertical wind speed nor its turbulent departure can be accurately obtained by the WS. This is why these values are “blank” in the PDS. Therefore, we use Monin-Obukhov similarity theory (G. Martínez et al., 2009; Monin & Obukhov, 1954) to calculate  $H_0$  as given in the following equation:

$$H_0 = k^2 U_a \rho_a c_p f(R_B) \frac{(T_g - T_a)}{\ln^2(z_a/z_0)}, \quad (2)$$

where  $k = 0.4$  is the Von Karman constant,  $U_a$  is the horizontal wind speed measured by the WS,  $\rho_a = P/(RT_a)$  is the air density derived from PS and ATS measurements, with  $R = 191 \text{ J kg}^{-1} \text{ K}^{-1}$  the Martian gas constant,  $z_a = 1.45$  is the height of the ATS and WS,  $z_0$  is the surface roughness (set to 1 cm; Hébrard et al., 2012), and  $f(R_B)$  is a function of the bulk Richardson number  $R_B = \frac{g}{T_g} \frac{(T_a - T_g) z_a}{U_a^2}$  defined as  $f(R_B) = (1 - 40R_B)^{1/3}$  if  $T_g > T_a$ , and  $f(R_B) = \max(0.007, \frac{1}{(1+5R_B+40R_B^2)^2})$  if  $T_g < T_a$ . This function accounts for the thermal stability in the first 1.45 m, and it has been tested under Earth Polar conditions (H. Savijärvi & Määttänen, 2010), which are reasonable environmental Mars analog.

The latent heat flux is defined as  $L_f = \rho_a L_v \left( \overline{w'q'} \right)_s$ , where  $L_v = 2.8 \times 10^6 \text{ J/Kg}$  is the latent heat of sublimation for water vapor, and  $q'$  is the turbulent departure of specific humidity (Garrat, 1992). As for  $H_0$ ,  $L_f$  has not been measured on Mars due to the lack of measurements of  $w'$  and  $q'$ . Nonetheless, this flux can be estimated using similarity theory and available measurements (see Equation 7 in G. M. Martínez et al., 2021). Due to the extremely low specific humidity values (Figure 3h) at the times when frost might have formed at Jezero (Hieta et al., 2022),  $L_f$  values are of the order of a few tenths of  $\text{W/m}^2$  or less, and thus can be neglected compared to the other terms of the SEB.

### 3.1.4. Net Heat Flux

The net heat flux into the ground is obtained from Equation 1, where all the terms on the right-hand side are calculated as explained in previous subsections. We note that fluxes in Equation 1 are referenced to a horizontal surface; however, fluxes measured by MEDA are referenced to Perseverance's local frame, the origin of which is located between the rover middle wheels and moves with the rover. In this local frame, +X is along the local north direction, +Z is along the downward normal at the landing site, and +Y completes the right-hand frame.

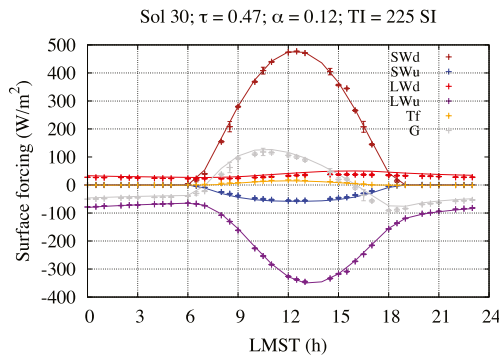


**Figure 4.** The surface energy budget on sol 30 ( $L_s \sim 20^\circ$ ) as a function of Local Mean Solar Times obtained from Mars Environmental Monitoring Station (MEDA) (symbols) and simulated with Single Column Model (SCM) (solid lines). Colors represent the terms of the surface energy budget in Equation 1. Except for the downwelling LW flux (red), which is systematically overestimated by the model, there is a very good agreement between observations and simulations. This behavior repeats on every other sol. SCM was run on sol 30 using the following values: visible aerosol opacity,  $\tau = 0.47$  (obtained from Mastcam-Z, Figure 3a), albedo at noon,  $\alpha = 0.12$  (obtained from MEDA), and thermal inertia,  $TI = 225 \text{ J m}^{-2} \text{ K}^{-1} \text{ s}^{-1/2}$ , which provides the best SCM fit to measured ground temperatures).

Using measurements of the rover's roll and pitch available in the PDS as “Ancillary Data” (\*DER Ancillary\* files), the inclination of the terrain traversed by the rover can be calculated as  $\sqrt{(\text{roll}^2 + \text{pitch}^2)}$  (Figure S4 in Supporting Information S1). However, this inclination is not necessarily the same as that of the terrain seen by the downward-looking TIRS channels (Figure 2), which is not known. For this reason, we do not attempt to correct measured fluxes for the inclination, and we simply assume that they are referenced to a horizontal frame. This is a reasonable approximation because between 10:00 and 14:00 LMST, when the solar flux is maximum, the ratio between fluxes referred to the local frame and a horizontal surface can be approximated by  $\mu_i/\mu_n$ , where  $\mu$  represents the cosine of  $SZA$ . Under this approximation, and given inclinations shown in Figure S4 in Supporting Information S1, most of the relative differences between fluxes stay below 5%, although they can be as large as  $\sim 20\%$  for extreme inclination values  $\sim 15^\circ$ .

Since MEDA measurements of the SEB are novel, we assessed them by comparing each term of Equation 1 with SCM-simulated values. We used SCM instead of COMIMART because while solar fluxes simulated by both models are nearly identical, only SCM can simulate LW fluxes. Figure 4 shows the terms of the SEB on sol 30 obtained from MEDA (symbols) and simulated with SCM (solid lines). On this sol, and on any other during the first 350 sols of the mission, the agreement between measurements and simu-

lations is very good for each term of the SEB except for  $LW_d$  (red), which is systematically overestimated by the model. This behavior and its implications are discussed in detail in Section 5.

### 3.2. Albedo

We determine the broadband hemispherical albedo (hereafter referred to as “albedo”) in the  $0.3\text{--}3 \mu\text{m}$  range as  $\alpha = SW_u^{0.3\text{--}3\mu\text{m}} / SW_d^{0.3\text{--}3\mu\text{m}}$ . Here,  $SW_u^{0.3\text{--}3\mu\text{m}}$  is the reflected solar flux in the  $0.3\text{--}3 \mu\text{m}$  band for a hemispherical FoV (available in the PDS as “CAL” values), and  $SW_d^{0.3\text{--}3\mu\text{m}}$  is the downwelling solar flux in the  $0.3\text{--}3 \mu\text{m}$  band for a hemispherical FoV, which is obtained following the same five steps enumerated in the first paragraph of Subsection 3.1.1.1, except for extending RDS/TOP7 measurements from  $0.19\text{--}1.2$  to  $0.3\text{--}3 \mu\text{m}$  (Data Set S2, fourth column). Based on uncertainties in measured solar fluxes, the relative error in albedo is  $<10\%$  in the vicinity of noon, and  $<20\%$  toward sunset and sunrise.

To obtain  $\alpha$  when the RDS/TOP7 was saturated (around noon between sols  $\sim 270$  and 350), we used COMIMART to simulate  $SW_d^{0.3\text{--}3\mu\text{m}}$  with aerosol opacity values from Mastcam-Z. Prior to sol 270 ( $L_s \sim 131^\circ$ ), relative differences between  $SW_d^{0.3\text{--}3\mu\text{m}}$  obtained from RDS/TOP7 and simulated by COMIMART are below 5% at LMSTs around noon, and therefore this is a reasonable approximation to calculate  $\alpha$  in the absence of RDS/TOP7 measurements.

In order to analyze the illumination and viewing geometry, we use contemporaneous “Ancillary” datafiles available in the PDS as “Derived Data.” In addition to the roll and pitch, these files contain values of the  $SZA$ , the solar azimuth angle ( $\phi_s$ ) relative to the M2020 local frame (defined as the angle between the positive  $X$ -axis and the orthogonal projection of the Sun onto the  $XY$  plane, with  $+90^\circ$  pointing West), and the rover's yaw ( $\phi_R$ ) relative to the M2020 local frame (defined as the counterclockwise rotation angle about the  $+Z$ -axis of the M2020 local level frame, with  $+90^\circ$  pointing East). The dependence of the albedo on the illumination and viewing geometry is shown in Section 4.3.

### 3.3. Thermal Inertia

For each sol when the rover was parked, we obtained thermal inertia ( $TI$ ) by solving the one-dimensional heat conduction equation for homogeneous terrains, Equation 3 (e.g., Garrat, 1992; Stull, 1988). We used MEDA

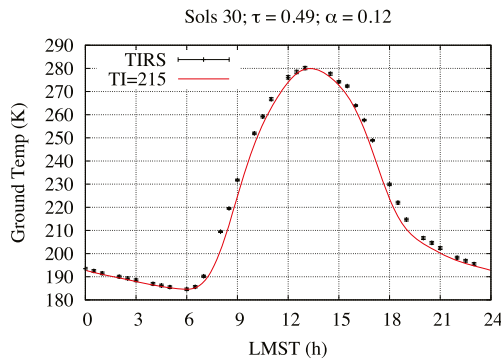


**Figure 5.** Ground temperature as a function of Local Mean Solar Times on sol 30 ( $L_s \sim 20^\circ$ ) measured by Thermal Infrared Sensor (black) and solved numerically from Equations 3–5 with a best-fitting value of  $TI = 215$  SI units. The cool bias in the numerical values during early and late daytime hours is caused by the assumption of homogeneous terrain, which we take in this study for the sake of simplicity. Note that the best-fitting value of  $TI$  obtained by Single Column Model (SCM) is 225 SI units (Figure 4). A similar good match in  $TI$  between SCM and MEDA observations (Equations 3–5) was obtained for other sols.

higher (lower)  $T_d$  values shift the solution  $T(z = 0, t)$  toward higher (lower) values,  $TI$  controls the diurnal amplitude (e.g., G. M. Martínez et al., 2014). Thus, there is only one pair of  $TI$  and  $T_d$  values that satisfy our imposed condition simultaneously.

To evaluate the uncertainty in  $TI$ , we performed sensitivity studies in Equations 3–5 by varying the values of  $\rho c$  between  $0.8 \times 10^6$  and  $1.6 \times 10^6 \text{ J m}^{-3} \text{ K}^{-1}$  (Grott et al., 2021; G. M. Martínez et al., 2014; Piqueux et al., 2021; Zent et al., 2010),  $z_d$  between  $2 \times L$  and  $4 \times L$ , and  $G$  between its maximum and minimum values based on uncertainties of the various terms on the right-hand side of Equation 1. We obtained relative variations in  $TI$  of  $\sim 2\%$  for the considered range of  $\rho c$  and  $z_d$ , and  $\sim 8\%$  for  $G$ . From these, we obtain an upper limit for the relative error in  $TI$  of  $\sim 10\%$ .

To validate our methodology for obtaining  $TI$ , we show in Figure 5 the ground temperature as a function of LMST on sol 30 ( $L_s \sim 20^\circ$ ) measured by TIRS (black) and numerically solved from Equations 3–5 with a best-fitting value of  $TI = 215$  SI units (red). The agreement is very good except for a cool bias in the numerical values (red) during early and late daytime hours. A similar behavior is found on other sols. This cool bias is explained by the assumption of homogeneous terrains, which we take in this study for the sake of simplicity and to obtain  $TI$  values without the need for thermal models. The reader is referred to H. I. Savijärvi et al. (2022) for further discussions of the heterogeneity of the terrain across Perseverance's traverse and its impact on the determination of thermal inertia and simulated ground temperatures.

## 4. Results

We show the results of thermal inertia in Section 4.1, which facilitate analyses of the surface energy budget presented in Section 4.2. Then, we show results of albedo in Section 4.3.

### 4.1. Thermal Inertia

Figure 6 (left) shows  $TI$  values for those of the first 350 sols of the M2020 mission where the rover was parked for at least an entire sol. Depending on the type of terrain,  $TI$  values ranged from 180 SI units on sol 106 (Figure 6, bottom right; sand dune) to 605 SI units on sol 125 (Figure 6, top right; bedrock-dominated material). This range of variation is nearly identical to that at the MSL landing site during the first 2,500 sols of that mission, with values between 170 and 610 SI units (Hamilton et al., 2014; G. M. Martínez et al., 2021; Vasavada et al., 2017).

$TI$  values varied less than  $\sim 8\%$  when the rover was parked in the same location for multiple sols (e.g., sols 138–152, 181–199, 211–237, or 249–276), consistent with the 10% relative error estimated for  $TI$ . An exception

measurements of the surface energy budget as the upper boundary condition, Equation 4, and a constant temperature  $T_d$  at a depth  $z_d$  as the lower boundary condition, Equation 5.

$$\frac{\partial T(z, t)}{\partial t} = \left( \frac{TI}{\rho c} \right)^2 \frac{\partial^2 T(z, t)}{\partial z^2} \quad (3)$$

$$-\left( \frac{TI^2}{\rho c} \right) \frac{\partial T(z = 0, t)}{\partial z} = G = SW_d - SW_u + LW_d - LW_u - H_0 - L_f \quad (4)$$

$$T(z = z_d, t) = T_d, \quad (5)$$

Here,  $\rho$  is the soil density,  $c$  the soil specific heat, and  $z_d$  is the diurnal penetration depth obtained as  $z_d = 3 \times \sqrt{(2/\omega)} \left( \frac{TI}{\rho c} \right)$ , where  $\omega = 7.0774 \times 10^{-5} \text{ s}^{-1}$  is the angular speed of the planet's rotation and  $L = \sqrt{(2/\omega)} \left( \frac{TI}{\rho c} \right)$  is the diurnal e-folding depth (see Section 4.2.1 in G. M. Martínez et al., 2014 for further information on  $z_d$  and  $T_d$ ).

Assuming a fixed value of  $\rho c = 1.2 \times 10^6 \text{ J m}^{-3} \text{ K}^{-1}$ ,  $TI$  and  $T_d$  are the only unknowns in Equations 3–5. By minimizing the difference between measured and numerically simulated values of the diurnal amplitude of ground temperature, the solution to Equations 3–5 is unique. This is because while

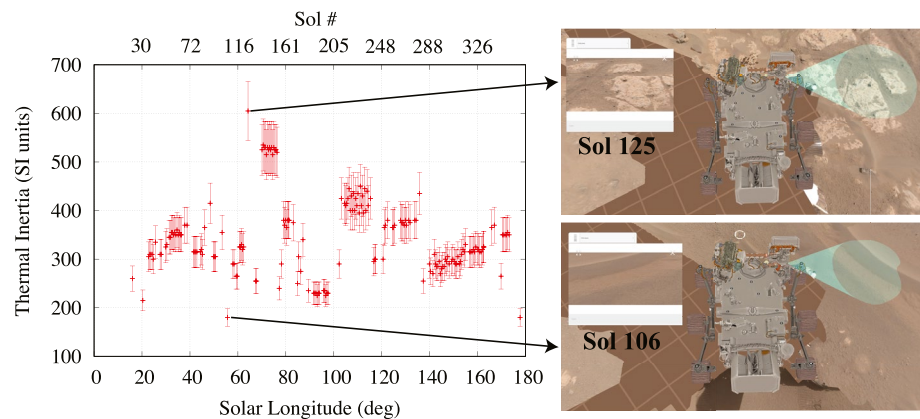


**Figure 6.** (left) Thermal inertia values for the first 350 sols of the M2020 mission when the rover was parked for an entire sol. (right) field of view of Thermal Infrared Sensor downward-looking channels (green shaded, ellipsoidal area of  $\sim 3\text{--}4\text{ m}^2$ ) on sols 125 (top) and 106 (bottom), corresponding to the terrains with the lowest (sand dune) and highest (bedrock-dominated material)  $TI$  values.

to this occurred during sols 287–328 (Ls  $\sim 140^\circ\text{--}161^\circ$ ), coinciding with the local dust storm on sols 312–318 (Ls  $152^\circ\text{--}156^\circ$ ). During this period,  $TI$  increased from an averaged value of 290 SI units on sols 287–312 to 315 SI units on sols 313–328 (Figure 6, left). Although this difference (25 SI units) is at the limit of the estimated uncertainty,  $TI$  values were repeatedly lower before the dust storm and repeatedly higher during and after. This suggests that the dust removal and sand transport which occurred on the FoV of TIRS during the dust storm (Vicente-Retortillo et al., 2022) might explain this behavior, as terrain with less dust would present higher  $TI$  values. In future work, we plan to evaluate the thickness of the dust layer consistent with the decrease in  $TI$ , and whether that thickness is realistic given the dust budget at the surface of Jezero.

As expected, terrains with higher (lower) values of  $TI$  underwent smaller (larger) diurnal amplitudes of ground temperature,  $\Delta T_g$  (Figure 3c). For instance, the relatively low  $TI$  (230 SI units) on sols 181–199 (Ls in  $90^\circ\text{--}97^\circ$ ) resulted in relatively large  $\Delta T_g \sim 87\text{ K}$ , while the relatively high  $TI$  (525 SI units) on sols 138–152 (Ls in  $70^\circ\text{--}76^\circ$ ) resulted in relatively low  $\Delta T_g \sim 56\text{ K}$ .

Figure 7 shows a thermal inertia map with values derived from MEDA (asterisks) and retrieved from the Thermal Emission Imaging System (THEMIS) on board the Mars Odyssey spacecraft (squares). Given the THEMIS' spatial resolution of 100 m per pixel (R. L. Fergason, Christensen, & Kieffer, 2006), we obtained THEMIS  $TI$  values as the average over  $0.001^\circ \times 0.001^\circ$  lon/lat boxes of three collocated stamps (“102413002,” “136033008,” and “145156005”) queried with the JMARS software and processed with the MARSTHERM model to derive  $TI$  values as a function of longitude and latitude (Mandon et al., 2020; Putzig & Mellon, 2007; Putzig et al., 2013).

While THEMIS retrievals ranged between 295 and 350 SI units across Perseverance's traverse, MEDA-derived values ranged between 180 and 605 SI units. These departures are caused by the different spatial resolution between both data sets ( $\sim 3\text{--}4$  vs.  $10^4\text{ m}^2$ ). Nonetheless, there is an overall good agreement between both data sets when  $TI$  averages over Perseverance's traverse is considered, with values of 350 SI units derived from MEDA, and 330 SI units derived from THEMIS.

For  $TI$  values below  $\sim 350$  SI units, the effective particle size of the surface can be estimated using an experimental relationship between the thermal inertia and the diameter ( $d$ ) of homogeneous spheres (Presley & Christensen, 1997):

$$d(\mu\text{m}) = \left( \frac{TI^2}{\rho c \times CP^{0.6}} \right)^{1/(-0.11 \log(P/K))} \quad (6)$$

Here,  $C = 0.0015$  and  $K = 8.1 \times 10^4$  torr are empirically derived constants,  $\rho c = 1.2 \times 10^6\text{ J m}^{-3}\text{ K}^{-1}$ , and  $P$  is the atmospheric pressure in torr. Using

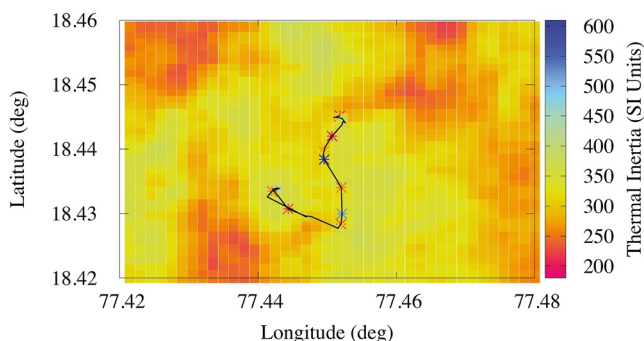


**Figure 7.** Color-coded thermal inertia map showing values retrieved from Thermal Emission Imaging System (THEMIS) (squares) and obtained from Mars Environmental Monitoring Station (MEDA) (asterisks). The black line represents the rover's traverse for the first 350 sols. While MEDA-derived  $TI$  values ranged between 180 and 605 SI units across the Perseverance's traverse (black line), THEMIS retrievals range between 295 and 350 SI units. These departures are caused by the different spatial resolutions of both data sets.

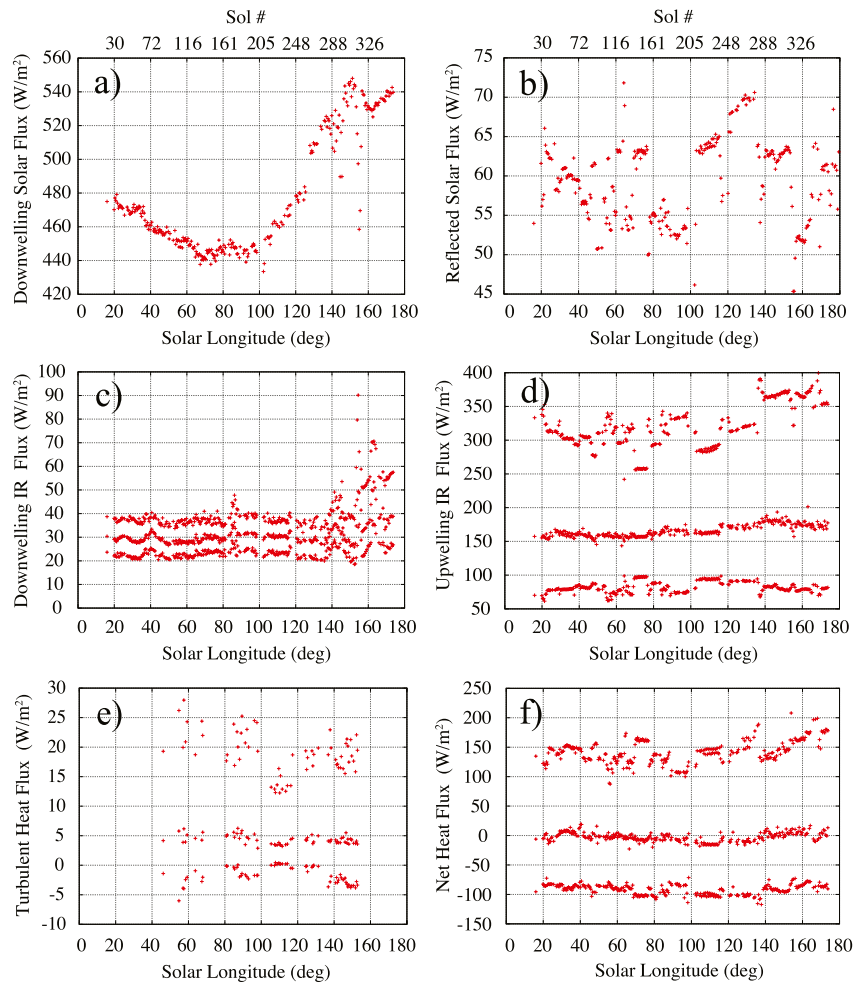


**Figure 8.** Surface energy budget at Jezero Crater as a function of  $L_s$  during the first 350 sols of the Mars 2020 mission. (a) Daily maximum downwelling solar flux ( $SW_d$ ; 0.19–5  $\mu\text{m}$ ). (b) Daily maximum reflected solar flux ( $SW_r$ ; 0.19–5  $\mu\text{m}$ ). (c) Daily maximum, mean, and minimum downwelling longwave flux ( $LW_d$ ; 5–80  $\mu\text{m}$ ). (d) Daily maximum, mean, and minimum upwelling longwave flux emitted by the surface ( $LW_u$ ; 5–80  $\mu\text{m}$ ). (e) Daily maximum, mean, and minimum turbulent heat flux ( $H_0$ ). (f) Daily maximum, mean, and minimum net heat flux into the ground ( $G$ ).

Equation 6,  $TI$  values from Figure 6 (left), and  $P$  values from Figure 3b (daily mean), we obtained particle sizes ranging from  $\sim 57 \mu\text{m}$  to almost 1 mm (Figure S5 in Supporting Information S1). As a future study, we plan to compare these values with particle sizes directly inferred from M2020 imagery, as well as to classify the geological type of terrain as a function of  $TI$ , albedo and grain size.

## 4.2. Surface Energy Budget

Figures 8 and 9 show the seasonal and diurnal evolution of each term of the SEB, respectively. We discuss each term below.

### 4.2.1. Shortwave Flux

The seasonal evolution of the daily maximum  $SW_d$  is shown in Figure 8a. During the aphelion season, when the aerosol opacity is low and relatively stable (Figure 3a), the seasonal evolution of  $SW_d$  is governed by the solar insolation at the top of the atmosphere (TOA, Figure S6 in Supporting Information S1). In particular,  $SW_d$  showed relative minimum at  $L_s \sim 65^\circ$  (same as in the TOA) and an absolute maximum at  $L_s \sim 150^\circ$ , when the aerosol opacity was relatively low (Figure 3a).  $SW_d$  decreased significantly during the regional dust storm that occurred on sols 312–318 ( $L_s 152^\circ$ – $156^\circ$ ), returning to prestorm values immediately after as the aerosol opacity decreased

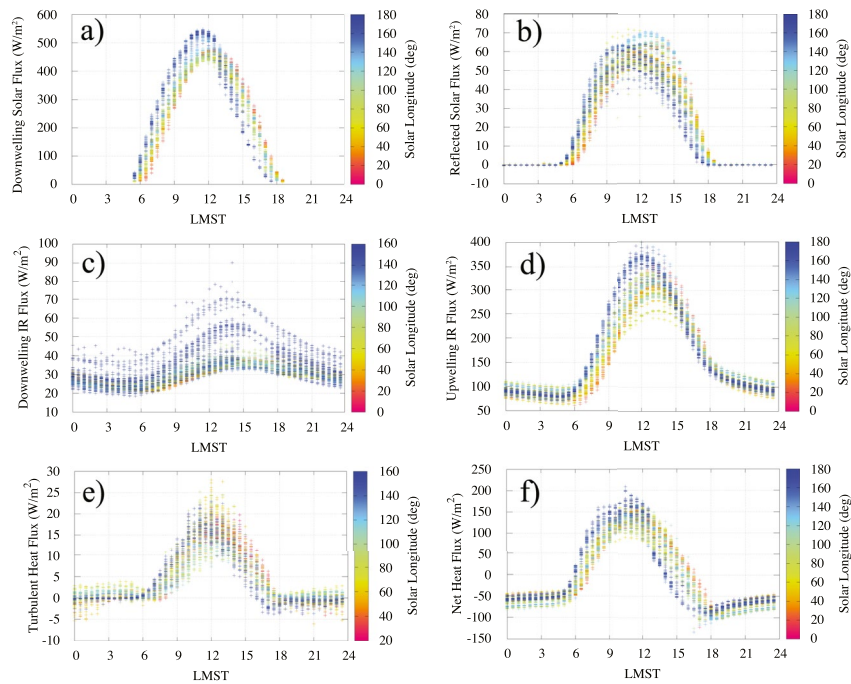


**Figure 9.** Diurnal evolution of the surface energy budget, Equation 1, at Jezero crater for the first 350 sols of the Mars 2020 mission. Color bar is used for Ls. Letters in each subpanel refer to the same term as in Figure 8.

(Lemmon et al., 2022). For comparison of  $SW_d$  with other landing sites, the reader is referred to G. M. Martínez et al. (2017).

The diurnal variation of  $SW_d$  is shown in Figure 9a. Daily maximum  $SW_d$  values typically occurred between 12:00 and 12:30 LMST for Ls in 20°–80° (first 160 sols; red-green colors), and between 11:00 and 12:00 LMST for Ls in 80°–180° (sols 160–350; green-blue colors). In addition to changes in the rover tilt and yaw, this behavior is mainly caused by differences between LMST and local true solar time (LTST), which range from around +30 min at the beginning of the mission to –40 min at Ls 180° (with LMST  $\approx$  LTST at Ls = 57° on sol 110).

The seasonal and diurnal evolution of  $SW_u$  are shown in Figures 8 and 9b, respectively.  $SW_u$  did not follow any particular trend in Ls, as it depends on the albedo of the terrain which changes along Perseverance's traverse. As for the diurnal variation, daily maximum  $SW_u$  values occurred between 10:00 and 14:00 LMST depending on the albedo, illumination and viewing geometry (more details in Section 4.3).

#### 4.2.2. Longwave Flux

The daily maximum, mean and minimum  $LW_d$  are shown in Figure 8c, with four relative maxima at Ls  $\sim$ 40° (sol 73), Ls  $\sim$ 86° (sol 174), Ls  $\sim$ 145° (sol 298), and Ls  $\sim$ 154° (sol 315; regional dust storm). To facilitate correlations with the opacity and thermal environment, Figure 10 shows color-coded values of  $LW_d$  (top), aerosol opacities at 9  $\mu$ m retrieved from TIRS IR1 and IR2 measurements with uncertainty of <0.02 (middle, Smith et al., 2022), and air temperature at about 40 m (bottom) as a function of Ls and LMST. The black arrows mark the Ls for each of the four relative maxima in  $LW_d$  in Figure 8c.

It follows from Figure 10 (middle) that each of these maxima were caused by periods of enhanced opacity. Interestingly, while opacity values retrieved from Mastcam-Z peaked at Ls  $\sim$ 145° and  $\sim$ 154°, they did not show particularly high values at Ls  $\sim$ 40° and  $\sim$ 86° (Figure 3a). This is because Mastcam-Z operates during the daytime, with most retrievals performed between 09:00 and 18:00 (Figure S2a in Supporting Information S1) when the aerosol opacity is relatively low (Figure 10 (middle)). Thus, the peaks in  $LW_d$  at Ls  $\sim$ 40° and  $\sim$ 86° occurred because opacity values stayed relatively high throughout those sols, with LMST periods of low opacity (purple and blue colors) narrower than in other surrounding Ls periods.

The diurnal variation of  $LW_d$ , which is the most complex among the SEB terms, is shown in Figures 9c and 10 (top). Typically, the daily maximum  $LW_d$  occurred between 13:00 and 16:00, and the daily minimum between

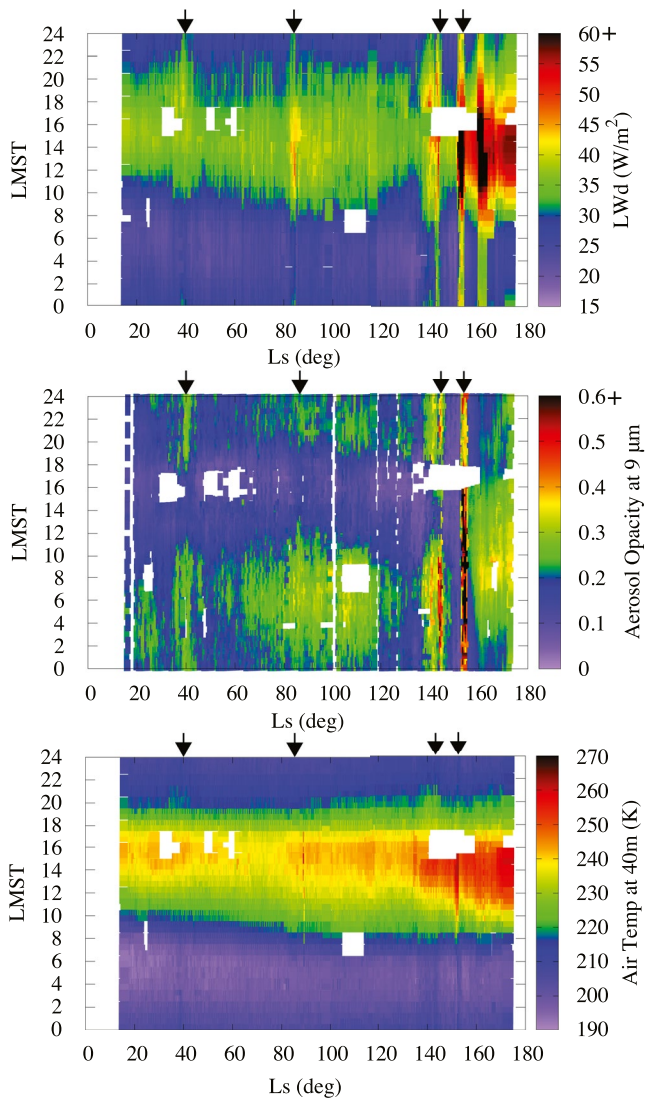


**Figure 10.** Color-coded downwelling LW flux (top), aerosol opacity at  $9 \mu m$  (middle), and air temperature at  $\sim 40 m$  (bottom) as a function of Ls and Local Mean Solar Times. The temporal gaps correspond to Thermal Infrared Sensor measurements taken either during in-flight calibrations or with the Sun within the FoV of IR1 and IR2. The black arrows mark the Ls at which the daily maximum, mean, and minimum  $LW_d$  showed relative maxima (Figure 8c).

04:00 and 06:00, roughly following the air temperature at  $\sim 40 m$  measured by TIRS/IR2 (Figure 10, bottom). However, the diurnal variation of  $LW_d$  is more complex than that of  $T_a$  at  $40 m$ , as it is also affected by aerosol opacity. As an example, Figure 11 (top) shows the diurnal variation of  $LW_d$  and  $\tau$  referenced at  $9 \mu m$  for sols 288 and 289 (Ls  $\sim 140^\circ$ ). Not only does  $LW_d$  present significantly different values on both sols, but the LMSTs at which the daily maximum and minimum  $LW_d$  are achieved are also different. These departures are caused by the diurnal evolution of  $\tau$  on both sols, with larger values and different LMST peaks on sol 298. However, the evolution of the air temperature at  $40 m$  on both sols was nearly identical (Figure 11, bottom). This is because while  $LW_d$  and  $\tau$  values are sensitive to the aerosol content and thermal profile in the entire atmospheric column,  $T_a$  values are determined by the thermal profile near the surface and are nearly insensitive to the aerosol content (Smith et al., 2022).

$LW_d$  was indirectly estimated at Gale crater using in situ measurements from the MSL/REMS instrument (G. M. Martínez et al., 2021). Between Ls  $20^\circ$  and  $150^\circ$ , daily mean values of  $LW_d$  ranged between 20 and  $40 W/m^2$  at Gale, in good agreement with values  $\sim 30 W/m^2$  observed at Jezero (Figure 8c). Between Ls  $150^\circ$  and  $180^\circ$ , the daily mean  $LW_d$  increased monotonically from 40 to  $60 W/m^2$  at Gale, while at Jezero, it also showed an upward trend from 30 to  $40 W/m^2$  following periods of enhanced opacity. As for the diurnal evolution,  $LW_d$  peaked between 15:00 and 16:00 LMST in the Ls  $0^\circ$ – $180^\circ$  period at Gale, in good agreement with Jezero (Figure 9c). A secondary  $LW_d$  peak was estimated at Gale between 06:00 and 09:00, which was likely attributed to inaccuracies in the estimation of  $LW_d$  (Figure 9 in G. M. Martínez et al., 2021). This secondary peak has not systematically appeared at Jezero, although the diurnal evolution of  $LW_d$  and  $\tau$  are complex, with strong sol-to-sol variability (Figure 11).

The daily maximum, mean and minimum  $LW_u$  is shown in Figure 8d. This quantity is a measure of the ground temperature (Figure 3c; Section 3.1.2.2.), and therefore strongly depends on the geophysical properties of the terrain, as well as on the solar flux reaching the surface. In particular, sol-to-sol variations are primarily caused by changes in the thermal inertia of the terrain (Figures 6 and 8d, left), while the seasonal evolution of the daily mean  $LW_u$  mostly follows that of  $SW_d$  (Figures 8d and 8a), with weak relative minimum at Ls  $\sim 65^\circ$  and a weak relative maximum at Ls  $\sim 150^\circ$ . Figure 9d shows the diurnal evolution of  $LW_u$ , with most of the daily maximum values occurring between 13:00 and 13:30 LMST for Ls in  $20^\circ$ – $80^\circ$  (first 160 sols; red-green colors), and between 12:00 and 13:00 LMST for Ls in  $80^\circ$ – $180^\circ$  (sols 160–350; green-blue colors). Based on differences between LMST and LTST ranging from +30 min at the beginning of the mission to  $-40$  min at Ls  $180^\circ$ , most daily maximum values of  $LW_u$  and  $T_g$  occurred around 13:00 LTST.

#### 4.2.3. Turbulent Heat Flux

Figure 8e shows the daily maximum, mean and minimum  $H_0$  on sols with complete diurnal WS coverage (Figure S1 in Supporting Information S1). Due to the thin Martian air ( $\rho_a \sim 10^{-2} kg/m^3$ ; Figure 3f),  $H_0$  shows the lowest maximum values among the SEB terms (excluding  $L_p$ ). The strong sol-to-sol variability in the daily maximum and minimum  $H_0$  is primarily caused by changes in the thermal gradient in the first 1.45 m (Equation 2), which in turn is driven by changes in the thermal inertia of the terrain, and, to a lesser extent, in the aerosol opacity content. For instance, daily maximum  $H_0$  values are lowest between Ls  $\sim 100^\circ$  and  $120^\circ$  (sols 211–237), when the rover was parked on a terrain with relatively high thermal inertia (Figure 6, left), and therefore relatively low thermal gradients in the first 1.45 m. Except for this long Ls period of relatively high  $TI$ , there seems to be a decreasing trend in  $H_0$  from Ls to  $60^\circ$ – $145^\circ$  (Figure 8e), which was likely caused by the contemporaneous decrease in atmospheric

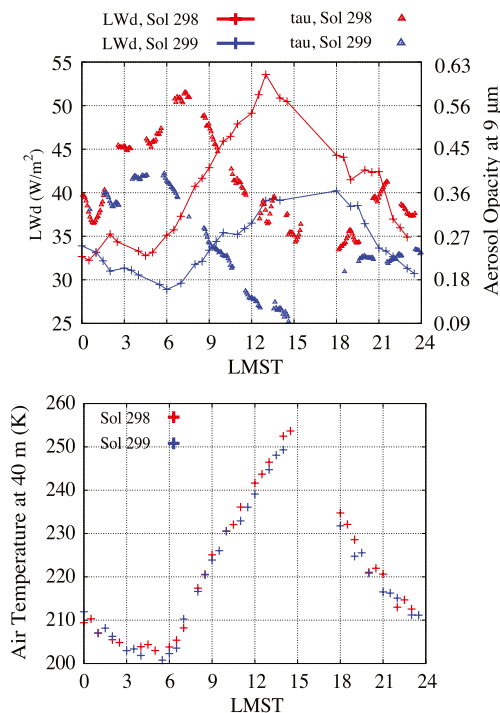


**Figure 11.** Diurnal evolution of the downwelling LW flux and aerosol opacity at  $9 \mu\text{m}$  (top), and the air temperature at  $\sim 40 \text{ m}$  (bottom) on sols 298 (red) and 299 (blue).  $LW_d$  values are connected with a colored line for the sake of clarity. While  $LW_d$  fluxes and  $\tau$  differ on both sols both quantitatively and qualitatively, the air temperature measured by Thermal Infrared Sensor (TIRS)/IR2 is similar. This is because TIRS/IR2 measurements are mainly determined by the thermal profile in the first few hundreds of meters (with the largest contribution from air layers at  $\sim 40 \text{ m}$ ), whereas  $LW_d$  and  $\tau$  are sensitive to the aerosol content and thermal profiles in the entire atmospheric column.

$LW_d$  via  $T_g$  (Figures 3c and 6 left, and Figure 8d). In particular, larger diurnal amplitudes in  $G$  typically resulted in higher  $TI$  values (Figure S7 in Supporting Information S1).

Figure 9f shows the diurnal variation of  $G$ . Positive values indicate heat conduction from the surface to the subsurface, while negative values indicate the reverse. For  $L_s$  in  $20^\circ\text{--}80^\circ$  (red-green colors), positive values typically occurred between  $\sim 07:00$  and  $\sim 15:00$  LMST, with daily maximum values at  $\sim 11:00$  LMST. For  $L_s$  in  $80^\circ\text{--}180^\circ$  (green-blue colors), positive values occurred between  $\sim 06:00$  and  $14:00$  LMST, with daily maximum values at  $\sim 10:30$  LMST. On the other hand, negative values typically peaked between  $18:00$  and  $19:00$  LMST for  $L_s$  in  $20^\circ\text{--}80^\circ$ , and between  $17:00$  and  $18:00$  LMST for  $L_s$  in  $80^\circ\text{--}180^\circ$ . This shift in  $L_s$  was mostly caused by differences between LMST and LTST. By comparing the diurnal variations in  $G$  (Figure 9f) and  $T_g$  (Figure S2c in Supporting Information S1), the daily maximum  $G$  typically occurred around 2 and 2.5 hr prior to the peak in  $T_g$ .

### 4.3. Albedo

Figure 13 (top) shows the whole set of MEDA-derived broadband ( $0.3\text{--}3 \mu\text{m}$ ) albedo values as a function of LMST during the  $L_s$  period in which the RDS/TOP7 was not saturated (first 270 sols). Only values with  $SZA < 60^\circ$  are shown to avoid large uncertainties close to sunrise and sunset. The two color-coded lines represent the albedo variation on sols 125 ( $L_s \sim 64^\circ$ ) and 209 ( $L_s \sim 102^\circ$ ), corresponding to the highest and lowest near-noon values during the first 270 sols. Figure S8 in Supporting Information S1 shows TIRS' FoV on these two sols.

The albedo presented a marked non-Lambertian behavior on every sol, with lowest values occurring near noon and highest toward sunrise and sunset. This is a common observation in Earth deserts (e.g., Zhang et al., 2014) and has been observed from in situ observations using the Viking and Mars Pathfinder landers (Guinness

density, as wind speeds did not show a marked seasonal variation (Figure 3f; Equation 2). A similar  $L_s$ -dependence was found at the landing site of the MSL mission, where  $H_0$  presented the highest seasonal values when the air density was highest (G. M. Martínez et al., 2021). It is unclear if a similar decreasing trend with  $L_s$  is also found in the vortex and dust devil activity observed by MEDA (Hueso et al., 2022).

The diurnal variation of  $H_0$  is shown in Figure 9e, with positive values when  $T_g > T_a$  and negative values when  $T_g < T_a$  (Equation 2). Positive values correspond to convective conditions ( $H_0$  directed from the surface to the atmosphere to cool down the surface), while negative values correspond to thermal inversions ( $H_0$  directed from the atmosphere toward the surface to warm it up). Typically, the daily maximum  $H_0$  occurred between  $11:00$  and  $13:00$  LMST, and the daily minimum occurred throughout  $18:00$  and  $06:00$ , following in both cases the diurnal trend of  $T_g - T_a$  (Figure 12, top). On some sols,  $T_g$  did not fall below  $T_a$  overnight and thus  $H_0$  stayed positive throughout the sol (Figure 12, top and Figure 9e). This lack of local thermal inversion mostly occurred on terrains with  $TI > 390$  SI units (Figure 12, bottom), which corresponded to localized terrains with  $TI$  values higher than the mean values across Perseverance's traverse obtained from MEDA (350 SI units) or THEMIS (330 SI units) (Section 4.1).

### 4.2.4. Net Heat Flux Into the Ground

The daily maximum, mean, and minimum net heat flux into the ground is shown in Figure 8f. The coverage for this term is better than for  $H_0$  because on sols without complete diurnal WS coverage, we obtained  $G$  from Equation 1 by calculating  $H_0$  values as the seasonal hourly average over the  $L_s$   $46^\circ\text{--}152^\circ$  (sols 85 and 313) period. This is a reasonable approximation given the lack of marked seasonal trend and low values of  $H_0$  during this period.

In the absence of abrupt changes in aerosol opacity (and thus in  $SW_d$  and  $LW_d$ ), the strong sol-to-sol variability in the daily maximum and minimum  $G$  (Figure 8f) was primarily caused by changes in thermal inertia and thus in

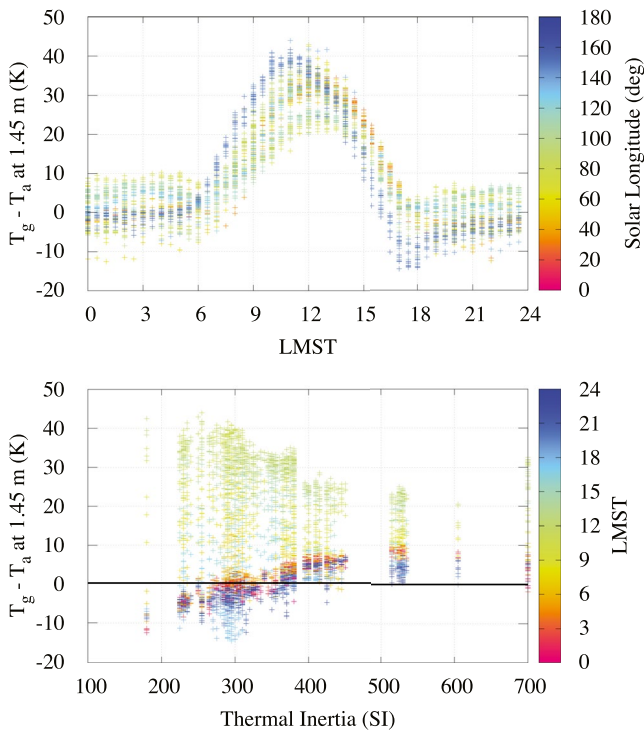


**Figure 12.** (top) Diurnal evolution of the thermal gradient in the first 1.45 m as a function of Local Mean Solar Times (LMST), with color code for  $L_s$ . This evolution governs the diurnal variation of the turbulent heat flux shown in Figure 9e. (bottom) Thermal gradient in the first 1.45 m as a function of thermal inertia, with color code for LMST. For  $TI > 390$  SI units, the ground temperature generally stayed warmer than the air at 1.45 m throughout the night (horizontal black line), indicating a lack of local thermal inversion.

et al., 1997; Johnson et al., 1999) the Mars Exploration Rovers (Johnson et al., 2006a, 2006b, 2021), and MSL (Johnson et al., 2022). To analyze the albedo as a function of the illumination and viewing geometry, we calculated values of the phase angle,  $\beta$ , defined as the angle between the incidence and emission vectors (Figure S9 in Supporting Information S1; Shepard, 2017):

$$\cos \beta = \cos(SZA)\cos(e) + \sin(SZA)\sin(e)\cos(\Delta\phi). \quad (7)$$

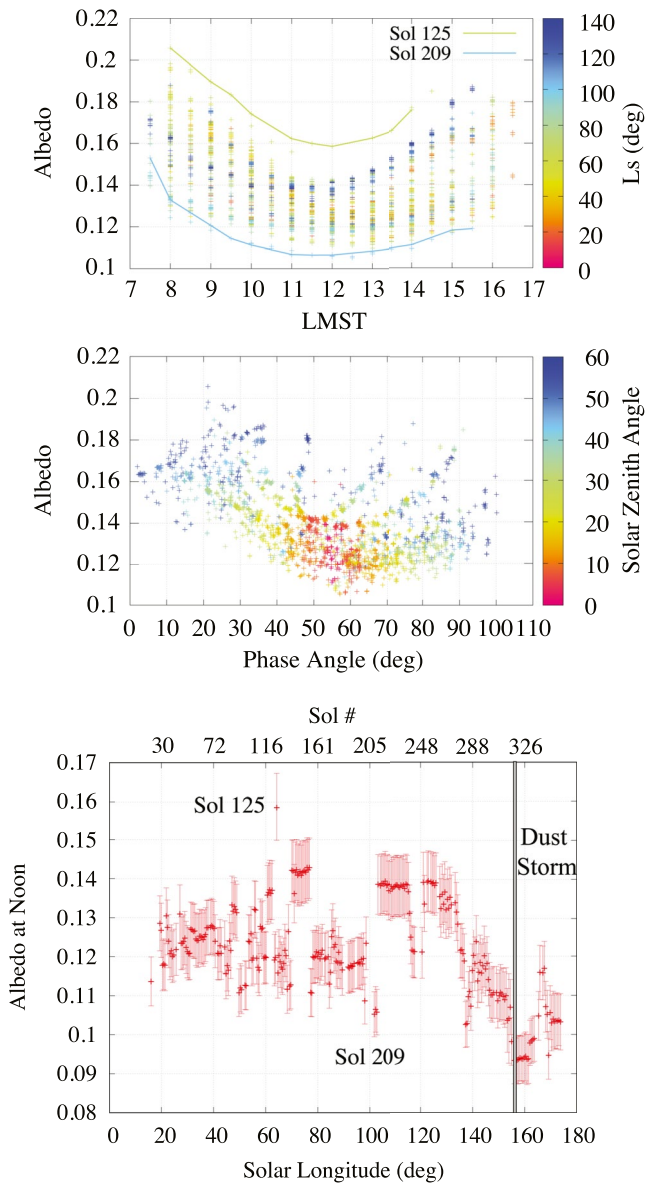
In Equation 7,  $SZA$  is the solar zenith angle,  $e$  is the emission angle between the surface normal and a vector to the observer ( $= 55^\circ$  given the  $-35^\circ$  pointing angle of TIRS/IR3; Table 1), and  $\Delta\phi = |\phi_s - \phi_{TIRS}| + 180^\circ$  is the difference between the solar azimuth angle,  $\phi_s$ , and the TIRS' azimuth angle,  $\phi_{TIRS}$ . This last angle is calculated from the rover's yaw,  $\phi_R$ , as  $\phi_{TIRS} = -\phi_R - 75^\circ$  by accounting for the opposite local frames used in the definition of  $\phi_s$  and  $\phi_R$  in the PDS, and the  $75^\circ$  of separation clockwise between the rover forward direction and TIRS (Section 3.2 and Figure 2). Low  $\beta$  values represent geometries when the Sun is directly behind TIRS' FoV, which occurs when TIRS is pointing toward East or West and  $SZA \sim 55^\circ$ . To illustrate this geometry, Figure S10 in Supporting Information S1 shows the diurnal evolution of the various angles involved in Equation 7 on sol 237, when the TIRS' FoV pointed approximately toward the East ( $\phi_{TIRS} = -102^\circ$ ).

Figure 13 (middle) shows the albedo as a function of the phase angle, with  $SZA$  represented using the color code. The highest albedo values correspond to low phase angles because of the overall backscattering nature of the Martian surface and the onset at smaller phase angles of the opposition effect. This occurs on surfaces when the Sun is directly behind the observer, and thus the shadows cast by their roughness elements (e.g., pores, pits) are minimized. The wider distribution of data points at the lowest phase angles likely represents variable inclusion of the rover mast's shadow in the TIRS' FoV. The upturn in the phase curves at  $\beta > 70^\circ$  demonstrates the forward scattering nature of some surfaces at high phase angles. Future work will

analyze individual phase angle curves as a function of the number and size of the scatterers in the TIRS' FoV (as determined by Mastcam-Z and/or Navcam images).

Figure 13 (bottom) shows the  $L_s$  evolution of the daily minimum  $\alpha$  for the first 350 sols of the mission, which ranged from 0.159 on sol 125 ( $L_s \sim 64^\circ$ ) to 0.093 on sol 318 ( $L_s \sim 156^\circ$ ). The daily minimum albedo varied less than 5% on sols when the rover was parked, consistent with an estimated relative error  $< 10\%$  (e.g., sols 138–152 and  $L_s 70^\circ$ – $76^\circ$ ; sols 181–199 and  $L_s 90^\circ$ – $98^\circ$ ; or sols 211–237 and  $L_s 103^\circ$ – $115^\circ$ ). As for thermal inertia, an exception to this occurred during the  $140^\circ$ – $161^\circ$   $L_s$  period (sols 287–328), which included the local dust storm on sols 312–318 ( $L_s 152^\circ$ – $156^\circ$ ). From the beginning of this period to the onset of the storm, near-noon albedo values decreased from around  $0.120 \pm 0.007$  to  $0.110 \pm 0.007$ . Then, during the storm, the albedo decreased to the lowest recorded values ( $0.093 \pm 0.006$ ), and it remained approximately constant until sol 328 ( $L_s \sim 161^\circ$ ), when the rover drove. The reader is referred to Vicente-Retortillo et al. (2022) for a detailed study of the decrease in albedo during the regional dust storm, which was found to be caused by dust removal and sand transport, and to Lemmon et al. (2022) for a detailed study of the environmental conditions during this storm.

Comparisons among albedo values retrieved in situ at different landing sites are problematic not only due to differences in the terrain but also in the technique used to obtain the albedo, the available LTSTs at which observations were acquired, and the general assumption of the Lambertian approximation in previous studies. Rice et al. (2018) derived a range of Pancam-derived Lambertian albedos ( $0.4$ – $1.0 \mu\text{m}$ ) of  $0.11$ – $0.22$  at Meridiani Planum (Opportunity, MER-B), and of  $0.14$ – $0.24$  at Gusev crater (Spirit, MER-A), with most of these observations acquired within 1 hr from local noon. Using numerical modeling and ground temperature measurements, Vasavada et al. (2017) and G. M. Martínez et al. (2021) estimated Lambertian albedo values in the  $0.06$ – $0.28$  range during the first 2,500 sols of the MSL mission. Using a similar technique, Piqueux et al. (2021) estimated a Lambertian albedo of  $0.16$  at the InSight landing site.



**Figure 13.** (top) Diurnal variation of broadband (0.3–3  $\mu\text{m}$ ) albedo for the first 270 sols of the mission, corresponding to color-coded  $L_s$  values between  $6^\circ$  and  $140^\circ$ . The two color-coded lines represent the albedo on sols 125 ( $L_s \sim 64^\circ$ ) and 209 ( $L_s \sim 102^\circ$ ), when the highest and lowest near-noon values were observed. (middle) Albedo as a function of phase angle and color-coded solar zenith angle. The brightest region corresponds to low phase angles. (bottom) Daily minimum (near-noon)  $\alpha$  as a function of  $L_s$  for the first 350 sols of the mission.

Bolometric albedos in the 0.25–2.9  $\mu\text{m}$  range have been retrieved from orbit by the Thermal Emission Spectrometer (TES) at around 14:00 LTST with a spatial resolution of  $\sim 300 \text{ km}^2$  and an uncertainty of 0.001. Figure 14 shows a map of MEDA-derived albedo values at  $\sim 14:00$  LMST (colored asterisks), with a greenish background color corresponding to a collocated TES-retrieved value of 0.147. While MEDA-derived values varied between  $\sim 0.10$  and 0.18 depending on the location, the averaged value across Perseverance's traverse was 0.14, in very good agreement with TES. Comparisons with bolometric albedos in the 0.25–2.9  $\mu\text{m}$  range retrieved from OMEGA with a spatial resolution between 1 and 2 km (Vincendon et al., 2015) are the subject of ongoing investigations.

## 5. Discussion: Atmospheric IR Flux

The agreement between MEDA observations and SCM simulations of each term of the SEB is quite good except for  $LW_d$  (Figure 4), which is systematically and significantly overestimated by SCM. To illustrate this behavior, Figure 15 shows the diurnal evolution of  $LW_d$  on sol 140 ( $L_s \sim 71^\circ$ ) observed by MEDA (red symbols) and simulated with SCM (solid black line). Also shown is the opacity retrieved from TIRS measurements (orange symbols; Smith et al., 2022), and retrieved from Mastcam-Z at  $\sim 17:22$  LTST (solid orange line). Note that TIRS-derived opacity values have been obtained at 9  $\mu\text{m}$ , but they are referenced here at 0.88  $\mu\text{m}$  by multiplying them by a factor of 1.8.

Discrepancies between observed and simulated  $LW_d$  values might be explained by the assumption made by SCM that aerosol opacity remains constant throughout the sol. While  $LW_d$  values simulated with SCM were obtained assuming a constant value of opacity given by Mastcam-Z,  $LW_d$  values observed by MEDA were retrieved in an environment with diurnally varying opacity values. As future work, we plan to analyze the impact of diurnally varying opacity on  $LW_d$ , both as simulated by SCM and as measured by MEDA.

Additionally, we plan to investigate the hypothesis that SCM presents a “warm” bias in  $LW_d$ . To test this, we plan to compare simulated values of  $LW_d$  from SCM and the Mars Climate Database (MCD) (Forget et al., 1999; Madeleine et al., 2011) built using the LMD Martian Atmospheric General Circulation Model. When diurnal variations in aerosol opacity are not considered, as it is the default in both models, preliminary results suggest that SCM values are systematically higher than LMD GCM values. This behavior seems to be caused by the fact that SCM does not include adiabatic cooling due to local uplift, whereas LMD GCM does. When adiabatic cooling is included in SCM,  $LW_d$  values provided by both models become similar. However, it remains to be assessed the sensitivity of both models to diurnally varying values of aerosol opacity, which neither SCM nor LMD GCM currently considers.

## 6. Summary and Conclusions

MEDA allows the determination of the surface radiative budget on Mars for the first time through measurements of the incident and reflected solar flux, the downwelling atmospheric IR flux, and the upwelling IR flux emitted by the surface. Moreover, MEDA allows the calculation of the broadband (0.3–3  $\mu\text{m}$ ) albedo through measurements of the incident and reflected solar flux for a variety of illumination and viewing geometries. It is important to assess the degree to which the surface materials depart from ideal Lambertian scattering. Although not directly,

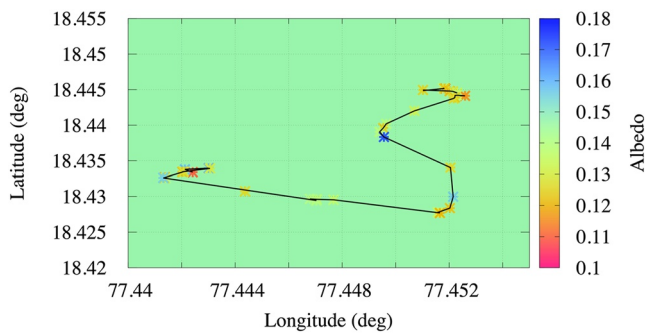


**Figure 14.** Color-coded albedo map showing Mars Environmental Monitoring Station (MEDA)-derived values at ~14:00 Local Mean Solar Times (asterisks) across Perseverance's traverse (black line), and a Thermal Emission Spectrometer (TES)-retrieved value of 0.147 (greenish background color) for the area shown at around the same local time. Although MEDA-derived values ranged between 0.1 and 0.18 depending on the terrain, the averaged MEDA-derived value across Perseverance's traverse was 0.14, which is in good agreement with TES.

MEDA also allows the estimation of the turbulent heat flux through measurements of ground and air temperature, horizontal wind speed, and atmospheric pressure. Thus, MEDA provides a good approximation to the surface energy budget at Jezero crater. Furthermore, MEDA allows the direct determination of thermal inertia for homogeneous terrains using measurements of the surface energy budget and ground temperature without the need for thermal numerical models.

Our main conclusions following the analysis of MEDA measurements for the first 350 sols of the M2020 mission are

1. Depending on the type of terrain, MEDA-derived  $TI$  values ranged between 180 (sand dune) and 605 (bedrock-dominated material) SI units. This range is nearly identical to that at the MSL landing site, with values between 170 and 610 SI units during the first 2,500 sols of that mission.
2. The range of variation of collocated THEMIS retrievals was significantly lower, with  $TI$  values between 295 and 350 SI units. However, there is a good agreement between both data sets when averages over Perseverance's traverse are considered, with values of 350 SI units derived from MEDA and 330 SI units derived from THEMIS. These departures are caused by the different spatial resolution between both data sets ( $\sim 3\text{--}4\text{ m}^2$  vs.  $10^4\text{ m}^2$ ).
3. There is a very good agreement between MEDA measurements and model (SCM) simulations of each term of the surface energy budget, except for the downwelling atmospheric IR flux. This term is systematically overestimated by SCM. This discrepancy might be caused by the strong diurnal variation in aerosol opacity measured by TIRS, which is not accounted for by numerical models (e.g., SCM). Alternatively, or in combination with the previous hypothesis, SCM might present a “warm” bias in  $LW_d$  because it does not include adiabatic cooling due to local uplift by default.
4. MEDA-estimated values of turbulent heat flux stayed positive through nighttime on certain sols, indicating a lack of thermal inversions. This occurred on sols with thermal inertia values significantly higher than the mean value across Perseverance's traverse obtained from MEDA (350 SI units) or THEMIS (330 SI units). This lack of local thermal inversion is explained by the small area covered by TIRS ( $3\text{--}4\text{ m}^2$ ), which measures ground temperatures not necessarily representative of the surroundings.
5. The albedo presented a marked non-Lambertian behavior on every sol, with lowest values occurring near noon and highest toward sunrise and sunset. The highest albedo values correspond to low phase angles because of the overall backscattering nature of the Martian surface and the onset at smaller phase angles of the opposition effect. The upturn in the phase curves at phase angles  $>70^\circ$  demonstrates the forward scattering nature of some surfaces at high phase angles.

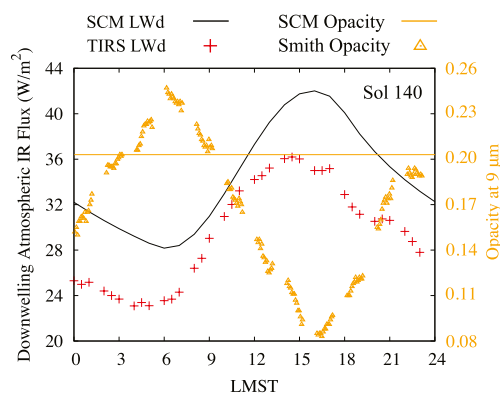


**Figure 15.** Diurnal evolution of the downwelling atmospheric IR flux observed by Mars Environmental Monitoring Station (MEDA) (red symbols) and simulated with Single Column Model (SCM) (black solid line) on sol 140 ( $L_s \sim 71^\circ$ ). The secondary  $Y$ -axis represents the aerosol opacity at  $0.88\ \mu\text{m}$  retrieved from Thermal Infrared Sensor (orange symbols), and retrieved from Mastcam-Z at  $\sim 17:22$  local true solar time (solid orange line). SCM-simulated  $LW_d$  values were obtained assuming a constant opacity given by Mastcam-Z, while MEDA-observed  $LW_d$  values were retrieved in an environment with diurnally varying opacity.

6. Depending on the type of terrain, the daily minimum albedo derived from MEDA ranged between 0.093 and 0.159. For comparison, Pancam-derived Lambertian albedos derived at the Opportunity and Spirit landing sites around local noon varied between 0.11–0.22 and 0.14–0.24, respectively. Using numerical modeling, Lambertian albedo values between 0.06 and 0.28 and of 0.16 were estimated at MSL and InSight, respectively. Thus, Jezero crater is among the darkest landing sites on Mars, in accordance with satellite estimations.
7. The lowest MEDA-derived albedo was recorded during the regional dust storm on sols 312–318 ( $L_s 152^\circ\text{--}156^\circ$ ), when values decreased dramatically due to dust removal and sand transport.
8. Collocated TES orbital retrievals of bolometric albedo in the  $0.25\text{--}2.9\ \mu\text{m}$  range, performed with a spatial resolution of  $\sim 300\text{ km}^2$  at around 14:00 LTST, showed a value of 0.147 at Jezero crater. While MEDA-derived values at around 14:00 LTST varied between  $\sim 0.10$  and 0.18 depending on the location, the averaged value across Perseverance's traverse was 0.14, in very good agreement with TES.

The following topics are left open for future investigations: (a) the apparent decrease in thermal inertia during the dust storm, (b) the classification of the geological type of terrain as a function of thermal inertia, albedo and grain size, (c) the analysis of individual phase angle curves as a function of the number and size of the scatterers in the TIRS' FoV (as determined by Mastcam-Z and/or Navcam images), (d) comparisons with bolometric albedos in the 0.25–2.9  $\mu\text{m}$  range retrieved from OMEGA with a spatial resolution between 1 and 2 km, and (e) analyses of the impact of diurnally varying opacity on  $LW_d$  and thermal profiles at diurnal and seasonal timescales, both as simulated by SCM and as measured by MEDA.

The results presented here are key to achieve MEDA's objectives within the M2020 mission, which are to validate model predictions and provide ground-truth to orbital measurements.

### Data Availability Statement

All Mars 2020 MEDA data necessary to reproduce each figure shown in this manuscript are available via the Planetary Data System (PDS) Atmospheres node (Rodríguez-Manfredi & de la Torre Juárez, 2021). An exception to this are the  $LW_d$  values in the 5–80  $\mu\text{m}$  range (Figures 8c, 9c, and 10 top, Figure 11 top, and Figure 15), and the aerosol opacity values derived from TIRS (Figure 10, middle and Figure 11, top), which are publicly available via the USRA Houston Repository (Martinez et al., 2022). THEMIS retrievals of thermal inertia shown in Figure 7 and TES retrievals of albedo in Figure 14 can be queried and processed using the open-source JMARS (Christensen et al., 2009) and MARSTHERM (Putzig et al., 2013) software.

### References

- Apéstigue, V., Gonzalo, A., Jiménez, J. J., Boland, J., Lemmon, M., de Mingo, J. R., et al. (2022). Radiation and dust sensor for Mars environmental dynamic analyzer onboard M2020 rover. *Sensors*, 22(8), 2907. <https://doi.org/10.3390/s22082907>
- Banfield, D., Spiga, A., Newman, C., Forget, F., Lemmon, M., Lorenz, R., et al. (2020). The atmosphere of Mars as observed by InSight. *Nature Geoscience*, 13(3), 190–198.
- Bell, J. F., III, Rice, M. S., Johnson, J. R., & Hare, T. M. (2008). Surface albedo observations at Gusev crater and Meridiani Planum, Mars. *Journal of Geophysical Research*, 113(E6), E06S18. <https://doi.org/10.1029/2007je002976>
- Chide, B., Bertrand, T., Lorenz, R. D., Munguira, A., Hueso, R., Sánchez-Lavega, A., et al. (2022). Acoustics reveals short-term air temperature fluctuations near Mars' surface. *Geophysical Research Letters*, 49(21), e2022GL100333. <https://doi.org/10.1029/2022gl100333>
- Christensen, P. R. (1988). Global albedo variations on Mars: Implications for active aeolian transport, deposition, and erosion. *Journal of Geophysical Research*, 93(B7), 7611–7624. <https://doi.org/10.1029/jb093ib07p07611>
- Christensen, P. R., Banfield, J. L., Hamilton, V. E., Ruff, S. W., Kieffer, H. H., Titus, T. N., et al. (2001). Mars Global surveyor thermal emission spectrometer experiment: Investigation description and surface science results. *Journal of Geophysical Research*, 106(E10), 23823–23871. <https://doi.org/10.1029/2000je001370>
- Christensen, P. R., Engle, E., Anwar, S., Dickensied, S., Noss, D., Gorelick, N., & Weiss-Malik, M. (2009). JMARS—a planetary GIS. In *AGU fall meeting Abstracts* (Vol. 2009, p. IN22A-06).
- Christian, J. R., Arvidson, R. E., O'Sullivan, J. A., Vasavada, A. R., & Weitz, C. M. (2022). CRISM-based high spatial resolution thermal inertia mapping along curiosity's traverses in Gale Crater. *Journal of Geophysical Research: Planets*, 127(5), e2021JE007076. <https://doi.org/10.1029/2021je007076>
- Creecy, E., Li, L., Jiang, X., Smith, M., Kass, D., Kleinböhl, A., & Martínez, G. (2022). Mars' emitted energy and seasonal energy imbalance. *Proceedings of the National Academy of Sciences of the United States of America*, 119(21), e2121084119. <https://doi.org/10.1073/pnas.2121084119>
- Edwards, C. S., Piqueux, S., Hamilton, V. E., Fergason, R. L., Herkenhoff, K. E., Vasavada, A. R., et al. (2018). The thermophysical properties of the Bagnold Dunes, Mars: Ground-truthing orbital data. *Journal of Geophysical Research: Planets*, 123(5), 1307–1326. <https://doi.org/10.1029/2017je005501>
- Elsasser, W. M. (1942). Heat transfer by infrared radiation in the atmosphere. *Harvard Meteor. Studies*, 6, 107.
- Farley, K. A., Williford, K. H., Stack, K. M., Bhartia, R., Chen, A., de la Torre, M., et al. (2020). Mars 2020 mission overview. *Space Science Reviews*, 216(8), 1–41. <https://doi.org/10.1007/s11214-020-00762-y>
- Fenton, L. K., Geissler, P. E., & Haberle, R. M. (2007). Global warming and climate forcing by recent albedo changes on Mars. *Nature*, 446(7136), 646–649. <https://doi.org/10.1038/nature05718>
- Fergason, R., Christensen, P., Golombek, M., & Parker, T. (2012). Surface properties of the Mars Science Laboratory candidate landing sites: Characterization from orbit and predictions. *Space Science Reviews*, 170(1–4), 739–773. <https://doi.org/10.1007/s11214-012-9891-3>
- Fergason, R. L., Christensen, P. R., Bell, J. F., III, Golombek, M. P., Herkenhoff, K. E., & Kieffer, H. H. (2006). Physical properties of the Mars Exploration Rover landing sites as inferred from Mini-TES-derived thermal inertia. *Journal of Geophysical Research*, 111(E2), E02S21. <https://doi.org/10.1029/2005JE002583>
- Fergason, R. L., Christensen, P. R., & Kieffer, H. H. (2006). High-resolution thermal inertia derived from the Thermal Emission Imaging System (THEMIS): Thermal model and applications. *Journal of Geophysical Research*, 111(E12), E12004. <https://doi.org/10.1029/2006je002735>
- Forget, F., Hourdin, F., Fournier, R., Hourdin, C., Talagrand, O., Collins, M., et al. (1999). Improved general circulation models of the Martian atmosphere from the surface to above 80 km. *Journal of Geophysical Research*, 104(E10), 24155–24175. <https://doi.org/10.1029/1999je001025>
- Garraat, J. R. (1992). *The atmospheric boundary layer*. Cambridge Atmos. Cambridge Univ. Press.
- Geissler, P. E., Fenton, L. K., Enga, M. T., & Mukherjee, P. (2016). Orbital monitoring of Martian surface changes. *Icarus*, 278, 279–300. <https://doi.org/10.1016/j.icarus.2016.05.023>
- Grott, M., Spohn, T., Knollenberg, J., Krause, C., Hudson, T. L., Piqueux, S., et al. (2021). Thermal conductivity of the Martian soil at the InSight landing site from HP<sup>3</sup> active heating experiments. *Journal of Geophysical Research: Planets*, 126(7), e2021JE006861. <https://doi.org/10.1029/2021je006861>

### Acknowledgments

Germán Martínez wants to acknowledge JPL funding from USRA Contract Number 1638782. A. V. R. is supported by the Spanish State Research Agency (AEI) Project MDM-2017-0737, Unidad de Excelencia “María de Maeztu”—Centro de Astrobiología (INTA-CSIC), and by the Comunidad de Madrid Project S2018/NMT-4291 (TEC2SPACE-CM). J. J. acknowledges funding from Mastcam-Z ASU subcontract 15-707. R. H., A. S. L., and A. M. were supported by Grant PID2019-109467GB-I00 funded by MCIN/AEI/10.13039/501100011033/ and by Grupos Gobierno Vasco IT1742-22. F. G. acknowledges financial support from the Agencia Estatal de Investigación of the Ministerio de Ciencia e Innovación and the European Regional Development Fund “A way of making Europe” through project the Centre of Excellence “María de Maeztu” award to the Centro de Astrobiología (MDM-2017-0737), and from the Instituto Nacional de Técnica Aeroespacial through Project S.IGS22001. L. M. was supported by CNES and IRIS-OCAV. J. P., M. H., and A.-M. H. are thankful for the Finnish Academy Grant 310509. M.-P. Z. was supported by Grant PID2019-104205GB-C21 funded by MCIN/AEI/10.13039/501100011033. M. de la T. J. acknowledges partial funding from the National Aeronautics and Space Administration (80NM0018D0004). The JPL co-authors acknowledge funding from NASA's Space Technology Mission Directorate and the Science Mission Directorate.

- Guinness, E. A., Arvidson, R. E., Clark, I. H., & Shepard, M. K. (1997). Optical scattering properties of terrestrial varnished basalts compared with rocks and soils at the Viking lander sites. *Journal of Geophysical Research*, *102*(E12), 28687–28703. <https://doi.org/10.1029/97je03018>
- Haberle, R. M., Houben, H. C., Hertenstein, R., & Herdtle, T. (1993). A boundary-layer model for Mars: Comparison with Viking lander and entry data. *Journal of the Atmospheric Sciences*, *50*(11), 1544–1559. [https://doi.org/10.1175/1520-0469\(1993\)050<1544:ablmfm>2.0.co;2](https://doi.org/10.1175/1520-0469(1993)050<1544:ablmfm>2.0.co;2)
- Hamilton, V. E., Vasavada, A. R., Sebastián, E., de la Torre Juárez, M., Ramos, M., Armiens, C., et al. (2014). Observations and preliminary science results from the first 100 sols of MSL Rover Environmental Monitoring Station ground temperature sensor measurements at Gale Crater. *Journal of Geophysical Research: Planets*, *119*(4), 745–770. <https://doi.org/10.1002/2013je004520>
- Hébrard, E., Listowski, C., Coll, P., Marticorena, B., Bergametti, G., Mänttinen, A., et al. (2012). An aerodynamic roughness length map derived from extended Martian rock abundance data. *Journal of Geophysical Research*, *117*(E4), E04008. <https://doi.org/10.1029/2011je003942>
- Hietala, M., Polkko, J., Jaakonaho, I., Genzer, M., Harri, A. M., Martínez, G. M., et al. (2022). First results of the relative humidity sensor on board M2020 perseverance rover. In *Seventh international workshop on the Mars atmosphere: Modelling and observations* (p. 3519).
- Hueso, R., Newman, C. E., del Rio-Gaztelurrutia, T., Munguira, A., Sanchez-Lavega, A., Toledo, D., et al. (2022). Convective vortices and dust devils detected and characterized by Mars 2020. *Journal of Geophysical Research: Planets*, *e2022JE007516*. <https://doi.org/10.1029/2022JE007516>. (under minor revisions; this issue).
- Johnson, J. R., Grundy, W., Lemmon, M. T., Liang, W., Bell, J. F., III, Hayes, A. G., & Deen, R. G. (2021). Spectrophotometric properties of materials observed by Pancam on the Mars exploration rovers: 4. Final mission observations. *Icarus*, *357*, 114261. <https://doi.org/10.1016/j.icarus.2020.114261>
- Johnson, J. R., Grundy, W., Lemmon, M. T., Liang, W., Bell, J. F., III, Hayes, A. G., & Deen, R. G. (2022). Spectrophotometric properties of materials observed by Mastcam on the Mars Science Laboratory at Gale Crater: 1. Bradbury landing to cooperstown. *Planetary and Space Science*, *222*, 105563. <https://doi.org/10.1016/j.pss.2022.105563>
- Johnson, J. R., Grundy, W. M., Lemmon, M. T., Bell, J. F., III, Johnson, M. J., Deen, R. G., et al. (2006a). Spectrophotometric properties of materials observed by Pancam on the Mars exploration rovers: 1. Spirit. *Journal of Geophysical Research*, *111*(E2), E02S14. <https://doi.org/10.1029/2005je002494>
- Johnson, J. R., Grundy, W. M., Lemmon, M. T., Bell, J. F., III, Johnson, M. J., Deen, R., et al. (2006b). Spectrophotometric properties of materials observed by Pancam on the Mars exploration rovers: 2. Opportunity. *Journal of Geophysical Research*, *111*(E12), E12S16. <https://doi.org/10.1029/2006je002762>
- Johnson, J. R., Kirk, R., Soderblom, L. A., Gaddis, L., Reid, R. J., Britt, D. T., et al. (1999). Preliminary results on photometric properties of materials at the Sagan Memorial Station, Mars. *Journal of Geophysical Research*, *104*(E4), 8809–8830. <https://doi.org/10.1029/98je02247>
- Kahre, M. A., Murphy, J. R., Chanover, N. J., Africano, J. L., Roberts, L. C., & Kervin, P. W. (2005). Observing the Martian surface albedo pattern: Comparing the AEOS and TES data sets. *Icarus*, *179*(1), 55–62. <https://doi.org/10.1016/j.icarus.2005.06.011>
- Kieffer, H. H., Martin, T. Z., Peterfreund, A. R., Jakosky, B. M., Miner, E. D., & Palluconi, F. D. (1977). Thermal and albedo mapping of Mars during the Viking primary mission. *Journal of Geophysical Research*, *82*(28), 4249–4291. <https://doi.org/10.1029/j082i028p04249>
- Lemmon, M. T., Smith, M. D., Viúdez-Moreiras, D., de la Torre-Juarez, M., Vicente-Retortillo, A., Munguira, A., et al. (2022). Dust, sand, and winds within an active Martian storm in Jezero Crater. *Geophysical Research Letters*, *49*(17), e2022GL100126. <https://doi.org/10.1029/2022gl100126>
- Madeleine, J. B., Forget, F., Millour, E., Montabone, L., & Wolff, M. J. (2011). Revisiting the radiative impact of dust on Mars using the LMD Global Climate Model. *Journal of Geophysical Research*, *116*(E11), E11101. <https://doi.org/10.1029/2011je003855>
- Maki, J., Thiessen, D., Pourangi, A., Kobzeff, P., Litwin, T., Scherr, L., et al. (2012). The Mars Science Laboratory engineering cameras. *Space Science Reviews*, *170*(1), 77–93. <https://doi.org/10.1007/s11214-012-9882-4>
- Maki, J. N., Bell, J. F., III, Herkenhoff, K. E., Squyres, S. W., Kiely, A., Klimesh, M., et al. (2003). Mars exploration rover engineering cameras. *Journal of Geophysical Research*, *108*(E12), 8071. <https://doi.org/10.1029/2003je002077>
- Mandon, L., Quantin-Nataf, C., Thollot, P., Mangold, N., Lozach, L., Dromart, G., et al. (2020). Refining the age, emplacement and alteration scenarios of the olivine-rich unit in the Nili Fossae region, Mars. *Icarus*, *336*, 113436. <https://doi.org/10.1016/j.icarus.2019.113436>
- Martínez, G., Valero, F., & Vázquez, L. (2009). Characterization of the Martian surface layer. *Journal of the Atmospheric Sciences*, *66*(1), 187–198. <https://doi.org/10.1175/2008jas2765.1>
- Martínez, G. M. (2022). Downwelling LW flux and aerosol opacity at Jezero Crater, Mars, as derived from MEDA/TIRS. Retrieved from <http://repository.hou.usra.edu/handle/20.500.11753/1839>
- Martínez, G. M., Newman, C. N., De Vicente-Retortillo, A., Fischer, E., Renno, N. O., Richardson, M. I., et al. (2017). The modern near-surface Martian climate: A review of in-situ meteorological data from Viking to curiosity. *Space Science Reviews*, *212*(1–2), 295–338. <http://doi.org/10.1007/s11214-017-0360-x>
- Martínez, G. M., Rennó, N., Fischer, E., Borlina, C. S., Hallet, B., De La Torre Juárez, M., et al. (2014). Surface energy budget and thermal inertia at Gale Crater: Calculations from ground-based measurements. *Journal of Geophysical Research: Planets*, *119*(8), 1822–1838. <https://doi.org/10.1002/2014je004618>
- Martínez, G. M., Vicente-Retortillo, A., Vasavada, A. R., Newman, C. E., Fischer, E., Rennó, N. O., et al. (2021). The surface energy budget at gale crater during the first 2500 sols of the Mars Science Laboratory mission. *Journal of Geophysical Research: Planets*, *126*(9), e2020JE006804. <https://doi.org/10.1029/2020je006804>
- Mellon, M. T., Jakosky, B. M., Kieffer, H. H., & Christensen, P. R. (2000). High-resolution thermal inertia mapping from the Mars global surveyor thermal emission spectrometer. *Icarus*, *148*(2), 437–455. <https://doi.org/10.1006/icar.2000.6503>
- Monin, A. S., & Obukhov, A. M. (1954). Osnovnye zakonomernosti turbulentnogo peremeshivaniya v prizemnom sloe atmosfery (Basic laws of turbulent mixing in the atmosphere near the ground). *Trudy Geofiz. Inst. AN SSSR*, *24*, 163–187.
- Montmessin, F., Gondet, B., Bibring, J. P., Langevin, Y., Drossart, P., Forget, F., & Fouchet, T. (2007). Hyperspectral imaging of convective CO<sub>2</sub> ice clouds in the equatorial mesosphere of Mars. *Journal of Geophysical Research*, *112*(E11), E11S90. <https://doi.org/10.1029/2007je002944>
- Munguira, A., Hueso, R., Sánchez-Lavega, A., de la Torre-Juarez, M., Martínez, G. M., Newman, C., et al. (2022). Mars 2020 MEDA measurements of near surface atmospheric temperatures at Jezero. In *Seventh international workshop on the Mars atmosphere: Modelling and observations* (p. 1509).
- Newman, C. E., Hueso, R., Lemmon, M. T., Munguira, A., Vicente-Retortillo, Á., Apestigue, V., et al. (2022). The dynamic atmospheric and aeolian environment of Jezero Crater, Mars. *Science Advances*, *8*(21), eabn3783. <https://doi.org/10.1126/sciadv.abn3783>
- Pérez-Izquierdo, J., Sebastián, E., Martínez, G. M., Bravo, A., Ramos, M., & Manfredi, J. A. R. (2018). The Thermal Infrared Sensor (TIRS) of the Mars Environmental Dynamics Analyzer (MEDA) instrument onboard Mars 2020, a general description and performance analysis. *Measurement*, *122*, 432–442. <https://doi.org/10.1016/j.measurement.2017.12.004>

- Piqueux, S., Müller, N., Grott, M., Siegler, M., Millour, E., Forget, F., et al. (2021). Soil thermophysical properties near the insight lander derived from 50 sols of radiometer measurements. *Journal of Geophysical Research: Planets*, 126(8), e2021JE006859. <https://doi.org/10.1029/2021je006859>
- Presley, M. A., & Christensen, P. R. (1997). The effect of bulk density and particle size sorting on the thermal conductivity of particulate materials under Martian atmospheric pressures. *Journal of Geophysical Research*, 102(E4), 9221–9229. <https://doi.org/10.1029/97je00271>
- Putzig, N. E., Barratt, E. M., Mellon, M. T., & Michaels, T. I. (2013). MARSTHERM: A web-based system providing thermophysical analysis tools for Mars research. In *AGU Fall Meeting Abstracts*, (Vol. 2013, p. P43C-2023).
- Putzig, N. E., & Mellon, M. T. (2007). Apparent thermal inertia and the surface heterogeneity of Mars. *Icarus*, 191(1), 68–94. <https://doi.org/10.1016/j.icarus.2007.05.013>
- Putzig, N. E., Mellon, M. T., Kretke, K. A., & Arvidson, R. E. (2005). Global thermal inertia and surface properties of Mars from the MGS mapping mission. *Icarus*, 173(2), 325–341. <https://doi.org/10.1016/j.icarus.2004.08.017>
- Rice, M. S., Reynolds, M., Studer-Ellis, G., Bell, J. F., III, Johnson, J. R., Herkenhoff, K. E., et al. (2018). The albedo of Mars: Six Mars years of observations from Pancam on the Mars exploration rovers and comparisons to MOC, CTX and HiRISE. *Icarus*, 314, 159–174. <https://doi.org/10.1016/j.icarus.2018.05.017>
- Rodríguez-Manfredi, J. A., & de la Torre Juárez, M. (2021). Mars 2020 perseverance rover Mars environmental Dynamics analyzer (MEDA) experiment data record (EDR) and reduced data record (RDR) data products archive bundle. *PDS Atmospheres Node*, 10, 1522849. <https://doi.org/10.17189/1522849>
- Rodríguez-Manfredi, J. A., De la Torre Juárez, M., Alonso, A., Apéstigue, V., Arruego, I., Atienza, T., et al. (2021). The Mars Environmental Dynamics Analyzer, MEDA. A suite of environmental sensors for the Mars 2020 mission. *Space Science Reviews*, 217(3), 1–86. <https://doi.org/10.1007/s1214-021-00816-9>
- Sánchez-Lavega, A., del Río-Gaztelurrutia, T., Hueso, R., de la Torre Juárez, M., Martínez, G. M., Harri, A. M., et al. (2022). Mars 2020 Perseverance rover studies of the Martian atmosphere over Jezero from 1 pressure measurements. *Journal of Geophysical Research: Planets*, 128(1), e2022JE007480. <https://doi.org/10.1029/2022JE007480>
- Savijärvi, H., & Määttä, A. (2010). Boundary-layer simulations for the Mars Phoenix lander site. *Quarterly Journal of the Royal Meteorological Society*, 136(651), 1497–1505. <https://doi.org/10.1002/qj.650>
- Savijärvi, H., Martínez, G., Harri, A. M., & Paton, M. (2020). Curiosity observations and column model integrations for a Martian global dust event. *Icarus*, 337, 113515. <https://doi.org/10.1016/j.icarus.2019.113515>
- Savijärvi, H. I., & Harri, A. M. (2021). Water vapor adsorption on Mars. *Icarus*, 357, 114270. <https://doi.org/10.1016/j.icarus.2020.114270>
- Savijärvi, H. I., Martínez, G., & Harri, A.-M. (2022). Surface energy fluxes and temperatures at Jezero Crater, Mars. *Journal of Geophysical Research: Planets*. <https://doi.org/10.1029/2022je007438>
- Sebastián, E., Armiens, C., Gomez-Elvira, J., Zorzano, M. P., Martínez-Frias, J., Esteban, B., & Ramos, M. (2010). The rover environmental monitoring station ground temperature sensor: A pyrometer for measuring ground temperature on Mars. *Sensors*, 10(10), 9211–9231. <https://doi.org/10.3390/s101009211>
- Sebastián, E., Martínez, G., Ramos, M., Haenschke, F., Ferrándiz, R., Fernández, M., & Manfredi, J. A. R. (2020). Radiometric and angular calibration tests for the MEDA-TIRS radiometer onboard NASA's Mars 2020 mission. *Measurement*, 164, 107968. <https://doi.org/10.1016/j.measurement.2020.107968>
- Sebastián, E., Martínez, G., Ramos, M., Perez-Grande, I., Sobrado, J., & Manfredi, J. A. R. (2021). Thermal calibration of the MEDA-TIRS radiometer onboard NASA's perseverance rover. *Acta Astronautica*, 182, 144–159. <https://doi.org/10.1016/j.actaastro.2021.02.006>
- Shepard, M. K. (2017). *Introduction to planetary photometry*. Cambridge University Press.
- Smith, M. D., Martínez, G. M., Sebastián, E., Lemmon, M. T., Wolff, M. J., Apéstigue, V., et al. (2022). Diurnal and seasonal variations of aerosol optical depth observed by MEDA/TIRS at Jezero Crater, Mars. *Journal of Geophysical Research: Planets*, e2022JE007560. <https://doi.org/10.1029/2022je007560>
- Smith, M. D., Wolff, M. J., Spanovich, N., Ghosh, A., Banfield, D., Christensen, P. R., et al. (2006). One Martian year of atmospheric observations using MER mini-TES. *Journal of Geophysical Research*, 111(E12), E12S13. <https://doi.org/10.1029/2006je002770>
- Spohn, T., Grott, M., Smrekar, S. E., Knollenberg, J., Hudson, T. L., Krause, C., et al. (2018). The Heat flow and physical properties package (HP3) for the InSight mission. *Space Science Reviews*, 214(5), 33. <https://doi.org/10.1007/s11214-018-0531-4>
- Stull, R. (1988). *An introduction to boundary layer meteorology* (p. 670). Springer.
- Sutton, J. L., Leovy, C. B., & Tillman, J. E. (1978). Diurnal variations of the Martian surface layer meteorological parameters during the first 45 sols at two Viking lander sites. *Journal of the Atmospheric Sciences*, 35(12), 2346–2355. [https://doi.org/10.1175/1520-0469\(1978\)035<2346:dvooms>2.0.co;2](https://doi.org/10.1175/1520-0469(1978)035<2346:dvooms>2.0.co;2)
- Toledo, D., Apéstigue, V., Arruego, I., Lemmon, M., Gómez, L., de Montoro, F., et al. (2023). Dust devil frequency of occurrence and radiative effects at Jezero Crater, Mars, as measured by MEDA Radiation and Dust Sensor (RDS). *Journal of Geophysical Research: Planets*. <https://doi.org/10.1029/2022JE007494>
- Vasavada, A. R., Piqueux, S., Lewis, K. W., Lemmon, M. T., & Smith, M. D. (2017). Thermophysical properties along Curiosity's traverse in Gale Crater, Mars, derived from the REMS ground temperature sensor. *Icarus*, 284, 372–386. <https://doi.org/10.1016/j.icarus.2016.11.035>
- Vicente-Retortillo, A., Martínez, G. M., Lemmon, M. T., Hueso, R., Sullivan, R., Newman, C. E., et al. (2022). Changes in surface albedo induced by dust devils and the MY 36 Ls 155 dust storm at Jezero Crater. In *Seventh international workshop on the Mars atmosphere: Modelling and observations* (p. 1512).
- Vicente-Retortillo, Á., Martínez, G. M., Renno, N., Newman, C. E., Ordóñez-Etxeberria, I., Lemmon, M. T., et al. (2018). Seasonal deposition and lifting of dust on Mars as observed by the Curiosity rover. *Scientific Reports*, 8(1), 1–8. <https://doi.org/10.1038/s41598-018-35946-8>
- Vicente-Retortillo, A., Martínez, G. M., Rennó, N. O., Lemmon, M. T., de la Torre-Juárez, M., & Gómez-Elvira, J. (2020). In situ UV measurements by MSL/REMS: Dust deposition and angular response corrections. *Space Science Reviews*, 216(5), 1–19. <https://doi.org/10.1007/s11214-020-00722-6>
- Vicente-Retortillo, Á., Valero, F., Vázquez, L., & Martínez, G. M. (2015). A model to calculate solar radiation fluxes on the Martian surface. *Journal of Space Weather and Space Climate*, 5, A33. <https://doi.org/10.1051/swsc/2015035>
- Vincendon, M., Audouard, J., Altieri, F., & Ody, A. (2015). Mars Express measurements of surface albedo changes over 2004–2010. *Icarus*, 251, 145–163. <https://doi.org/10.1016/j.icarus.2014.10.029>
- Viúdez-Moreiras, D., de la Torre, D., Gómez-Elvira, J., Lorenz, R. D., Apéstigue, V., Guzewich, S., et al. (2022). Winds at the Mars 2020 landing site. Part 2: Wind variability and turbulence. *Journal of Geophysical Research: Planets*. e2022JE007523. <https://doi.org/10.1029/2022JE007523>
- Viúdez-Moreiras, D., Lemmon, M., Newman, C. E., Guzewich, S., Mischna, M., Gómez-Elvira, J., et al. (2022). Winds at the Mars 2020 landing site. Part 1: Near-surface wind patterns at Jezero Crater. *Journal of Geophysical Research: Planets*. e2022JE007522. <https://doi.org/10.1029/2022JE007522>

- Wolff, M. J., López-Valverde, M. I. G. U. E. L., Madeleine, J. B., Wilson, R. J., Smith, M. D., Fouchet, T., & Delory, G. T. (2017). Radiative process: Techniques and applications. *The Atmosphere and Climate of Mars*, 18, 106.
- Zent, A. P., Hecht, M. H., Cobos, D. R., Wood, S. E., Hudson, T. L., Milkovich, S. M., et al. (2010). Initial results from the thermal and electrical conductivity probe (TECP) on Phoenix. *Journal of Geophysical Research*, 115(E3), E00E14. <https://doi.org/10.1029/2009je003420>
- Zhang, Y. F., Wang, X. P., Hu, R., Pan, Y. X., & Zhang, H. (2014). Variation of albedo to soil moisture for sand dunes and biological soil crusts in arid desert ecosystems. *Environmental Earth Sciences*, 71(3), 1281–1288. <https://doi.org/10.1007/s12665-013-2532-7>